Quantum dynamics and cooling of atoms in one-dimensional standing-wave laser fields: Anomalous effects in Doppler cooling

M. R. Doery, E. J. D. Vredenbregt,* and T. Bergeman
Physics Department, State University of New York, Stony Brook, New York 11794-3800
(Received 26 October 1994)

We report computational results for the time evolution of the velocity distribution $P(V,t)$ for two-level and multilevel "Doppler" laser cooling. We compare results obtained from the semiclassical (SC) Fokker-Planck equation and from generalized optical Bloch equations applied to density matrices over a basis of products of internal and quantized translational states (QDM). Computer memory requirements are optimized to make large-scale QDM calculations feasible. QDM and SC agree well except for two cases: (a) atoms in the wells of the light-shift potential (with kinetic energy less than the well depth, U_0), and (b) atoms with recoil energy E_R comparable to or greater than the natural linewidth $\hbar\Gamma$. Transient dips occur in $P(V,t)$ at $V = 0$ in QDM results due to slow cooling of atoms in the light-shift potential wells. Dips in $P(V,t)$ occur at velocity-tuned-resonance (Doppleron) velocities but disappear over long interaction times as atoms accumulate near points where the force is zero. When $E_R \approx \hbar\Gamma$, sharp peaks occur in $P(V,t)$ at $V = \pm V_R$ from velocity-selective population quasitrapping not previously found in a two-level transition. Sharp features in $P(V,t)$ occur also for $J \rightarrow J+1$ transitions with $J > 0$, small U_0/E_R, and sufficiently large detuning, from transitions between individual quantum states in the periodic potential.

PACS number(s): 32.80.Pj, 42.50.Vk

I. INTRODUCTION

Dynamic effects in the interaction between atoms and laser fields are now known to produce many interesting and useful phenomena, most notably atom cooling, atom trapping, and localization of atoms in standing-wave nodes or antinodes [1–4]. The conditions for achieving the lowest steady-state temperatures in Doppler [5–7], sub-Doppler [8,9], and velocity-selective coherent population trapping (VSCPT) methods [10,11] have been extensively discussed. However, when performing experiments under diverse conditions, it is useful to understand the broad range of dynamic processes that can occur when atoms interact with laser light. Laser detuning and intensity may deviate from optimum or the laser-atom interaction time may be too short for the steady state to be attained, as is easily the case for transverse cooling of an atomic beam. Transient phenomena and large-recoil effects can provide a sensitive probe of the dynamics of laser-atom interactions and of quantized motion of atoms in the periodic light-shift potential wells.

Three basic theoretical methods have been developed to deal with these questions. (a) The semiclassical (SC) method [12–17] uses spatially averaged force and diffusion functions in a Fokker-Planck equation or Langevin equation for the velocity distribution. Both of these assume [17,18] that the momentum increments ($\hbar k$) from photon recoil are small compared with the momentum width ($\sqrt{2M\hbar\Gamma}$), hence that the recoil energy $E_R \equiv \hbar^2k^2/2M \ll \hbar\Gamma$, where $k = 2\pi/\lambda$, M is the atomic mass, and Γ is the spontaneous radiative decay rate. The SC method is by far the most economical for computer memory and CPU time, but the effect of the limiting assumptions (spatial averaging and small momentum increments) on calculated velocity distributions has not been spelled out. (b) The quantum density matrix (QDM) method [9,6,19–23] uses a product of quantized internal and translational states in a Liouville density matrix equation. Since laser cooling problems usually require a large number of momentum states, the major limitation of this method has been the size of the computer memory required to handle a density matrix of order $\mathfrak{N}^2$ for $\mathfrak{N}$ basis states, where $\mathfrak{N}$ is the product of the number of internal and translational states. (c) The quantum Monte Carlo (QMC) [24–26] method uses statistical realizations of solutions of the Schrödinger equation, which requires a calculation over just the $\mathfrak{N}$ basis states, rather than over $\mathfrak{N}^2$ density matrix elements. Reducing the statistical noise enough to see details in $P(V,t)$, however, requires many realizations and relatively large amounts of CPU time.

In this study, we report results of calculations with SC and QDM methods of the temporal evolution of the velocity distribution $P(V,t)$ in two-level Doppler cooling over a wide range of laser and atomic parameters, and for Doppler cooling of atoms with multiple sublevels with weak excitation. The objective of our work is to help identify and interpret experimental observations and to indicate under what conditions various phenomena occur. The experimental context we address is transverse laser cooling of an atomic beam, as in experiments on lithium atoms in which velocity-tuned resonances (Dopplerons) were observed [27], and also in recent experiments on He atoms [23], in which effects of quantized motion were observed in the velocity distribution. Our discussion considers $J \rightarrow J+1$ transitions in a $\sigma^+ - \sigma^+$ standing-wave laser field. (J is the total angular momentum of the

*Present address: Physics Department, Eindhoven University of Technology, P.O. Box 513, 5600 MB Eindhoven, The Netherlands.

ground state of the atom. When there is nuclear spin, it is commonly denoted F.) For $J = 0$ one has simply two-level cooling on the $m = 0 \rightarrow 1$ transition component, while the case of $J = 1/2$ brings in additional phenomena that can occur in atoms with degenerate sublevels. For simplicity, we assume a flat (rectangular) initial velocity distribution for $|V| \leq V_{\max}$. A second report will discuss the quantum effects observable in the velocity distribution in Sisyphus sub-Doppler cooling such as those reported in Ref. [23].

We will show (Sec. II, especially Sec. II C, and Sec. III F) that computational optimization can drastically reduce the memory and CPU requirements of the QDM approach. At least for two-level problems in one dimension, these optimized QDM methods now typically require less CPU time than QMC methods to obtain comparable detail in features in the velocity distribution [28,29]. Detailed comparisons reveal good agreement between results from SC and QDM methods over a wide range of parameters, giving credibility to both of these very different methods, and justifiying use of the much faster SC methods for many conditions. The major differences between SC and QDM results occur when atom kinetic energies are less than the well depth of the periodic light-shift potential ($E_K < U_0$), when the recoil energy is comparable to or larger than the radiative linewidth ($E_R \gtrsim \hbar\Gamma$), or when quantum interference effects are present (for $E_R \gtrsim \hbar\Gamma$).

Since the original proposals [30,31], Doppler cooling has been addressed theoretically many times [5,6,12,26,32,33]. With the computational methods outlined in Sec. II, we examine in Sec. III several effects not emphasized in previous discussions of the velocity distribution. By way of introduction, we show the effects of varying $E_R/\hbar\Gamma$ when SC force and diffusion functions are kept constant (Sec. III A), and effects of larger than optimum detuning or intensity (Sec. III B). We then focus on a significant and general conclusion from the QDM calculations: Slower cooling of atoms in the wells of the periodic light-shift potential produces a deficiency of atoms near zero velocity. This effect was discussed from the point of view of classical trajectories by Bigelow and Prentiss [34], but there was no calculation of the expected effect on $P(V,t)$. Localization effects have been discussed theoretically also for lin $\perp$ lin cooling (two counterpropagating laser beams with orthogonal linear polarization) [9,35] and in Ref. [16] for a special one-dimensional (1D) cooling model. For 1D Doppler cooling, we find that there is often a transient dip in $P(V,t)$ at $V = 0$ (as observed experimentally in Ref. [23]), and that even in the steady state, the SC amplitude of $P(V,t)$ at $V = 0$ tends to be larger than the QDM amplitude. Our calculations of the spatial distribution $P(z,t)$ show that after a short time for which there is a small surplus of atoms at the nodes of the laser field, up to 22% more atoms are found at the laser antinodes (potential minima for red detuning) than at the nodes. This is substantially less than expected for a thermal distribution in the periodic light-shift potential.

To put this effect in a broader perspective, we point out other circumstances that can lead to superficially similar results for $P(V,t)$. For example, with large detuning, atoms accumulate temporarily in peaks with $|V| \neq 0$. Until these peaks eventually coalesce into a single peak at $V = 0$, one has the appearance of a dip at $V = 0$ between them. Also, at high laser intensity (Sec. III D), the slope of the force versus velocity function changes sign at $V = 0$, and one has the regime of "blue cooling" or "red heating" [36]. A dip at $V = 0$ in $P(V,t)$ results from the latter. These last two effects can be obtained with the Fokker-Planck equation, but the effect of slower cooling in the wells is associated with spatial variations of velocity, force, and atom density, for which the Fokker-Planck equation becomes difficult to solve.

Doppleron resonances were discussed some time ago by Berman and Ziegler [37], Kyrölä and Stenholm [38], and Minogin and Serimaa [39], who showed that peaks in the force function and in the population difference between ground and excited states occur when successive increments of kV combine to produce resonances at approximately $\delta = (2j+1)kV$ where δ is the detuning and j is an integer. Hulet and co-workers [27] and Bigelow and Prentiss [40] have reported experimental observations. Carrying these previous efforts further, our calculations (Sec. III D) display the full time evolution of Doppleron resonance dips in $P(V,t)$, and show that these dips eventually disappear as the atoms accumulate near velocities where the force is zero.

In Sec. III E, we consider recoil energies comparable to or larger than the natural linewidth, where the assumptions of semiclassical theory are violated. Castin *et al.* [6] have discussed this regime of Doppler cooling for the special case of a $\sigma^+ - \sigma^-$ polarized standing wave, in which there are closed three-member families of states. For $\sigma^+ - \sigma^+$ standing-wave laser fields, the families are not closed, and the results differ. The most striking features in the calculated $P(V,t)$ distributions in this regime are the quasi-VSCPT peaks due to suppressed decay of states that involve a linear superposition of $V = \pm V_R$ ground states. This phenomenon has not been noted previously for two-level atoms, and is most significant when $E_R \approx \hbar\Gamma/2$.

Having reviewed several anomalous effects in two-level Doppler cooling, we are able to identify additional effects resulting from optical pumping among multiple degenerate sublevels (Sec. IV). The most visible effects occur when the depth of the light-shift potential wells is not more than a few times the recoil energy E_R. In this case, there are only a few bands of Bloch states in the sinusoidal periodic light-shift potential, and the very lowest bands play a significant role. The first band gap, where the wave functions have the same period as the laser, is particularly important. The transition elements can vary within the lowest band, and the rapid depopulation of the lowest band or bands of the $m < J$ manifolds can produce characteristic transient features in $P(V,t)$.

II. THEORETICAL METHODS

A. Hamiltonian terms and definitions

The optical Bloch equation (Liouville equation) for the density matrix ρ is

$$\dot{\rho} = -\frac{i}{\hbar}[H,\rho] + \dot{\rho}_{\rm SE} + \dot{\rho}_{\rm repop}. \quad (1)$$

We have separated radiative decay into two terms which have quite different forms. $\dot{\rho}_{\rm SE}$ expresses the spontaneous emission loss rates for excited-state elements and ground-excited coherences, while $\dot{\rho}_{\rm repop}$ gives the gain rates for ground-state elements from repopulation effects. The Hamiltonian H includes terms for the center-of-mass kinetic energy, internal atomic electronic energy, and the laser-atom interaction:

$$\begin{aligned} H &= H_{\rm KE} + H_A + H_{AL} \\ &= \frac{\hat{P}^2}{2M} + \hbar\omega_0 \sum_i |e_i\rangle\langle e_i| - \mathbf{E}(\mathbf{r},t)\cdot\mathbf{d}. \end{aligned} \quad (2)$$

$\hat{P}$ is the momentum operator, ω_0 the atomic excitation frequency, and the sum is over excited-state sublevels. In the rotating wave approximation, which removes the time dependence from H_{AL}, ω_0 is replaced with $-\delta = -\omega+\omega_0$, where δ is the detuning, and ω is the laser frequency. In this discussion, we consider optical fields consisting of counterpropagating beams with identical circular polarization and $J \to J+1$ transitions only, where J denotes the total angular momentum of the ground state ($J \to J$ and $J \to J-1$ transitions typically involve special effects associated with dark states).

If each beam is σ^+ circularly polarized, then the laser electric field $\mathbf{E} = \sum_\sigma (E_\sigma^+ e^{-i\omega t} + E_\sigma^- e^{i\omega t})\hat{\boldsymbol{\epsilon}}_{-\sigma}(-1)^\sigma$ may be written

$$\begin{aligned} \mathbf{E} &= \frac{1}{\sqrt{2}} E_L \{\hat{\mathbf{x}}[\cos(kz+\omega t) + \cos(kz-\omega t)] \\ &\quad + \hat{\mathbf{y}}[\sin(kz+\omega t) - \sin(kz-\omega t)]\} \\ &= -\hat{\boldsymbol{\epsilon}}_+ E_L \cos(kz) e^{-i\omega t} + \text{c.c.}, \end{aligned} \quad (3)$$

so that $E_\pm^\pm = E_0^\pm = 0$ and $E_\pm^\mp = \mp E_L \cos(kz)$ in this case. The time average for each beam is $\langle \mathbf{E}^2\rangle = E_L^2/2$, as for a linearly polarized beam of the form $\hat{\mathbf{x}} E_L \sin(kz-\omega t)$. We have used $\hat{\boldsymbol{\epsilon}}_\pm = \mp(\hat{\mathbf{x}} \pm i\hat{\mathbf{y}})/\sqrt{2}$.

In evaluating $H_{AL} = -\mathbf{E}\cdot\mathbf{d} = -\sum_\sigma (-1)^\sigma (E_{-\sigma}^+ d_\sigma^+ e^{-i\omega t} + E_{-\sigma}^- d_\sigma^- e^{i\omega t})$, we denote by d_σ^+ (d_σ^-) a raising (lowering) operator. In computing adjoint elements, one has the relation $(d_\sigma^+)^\dagger = (-1)^\sigma d_{-\sigma}^-$. Elements of the dipole moment operator are, for example,

$$\langle e, J+1, m_g+\sigma | d_\sigma^+ | g, J, m_g\rangle = \langle J+1, m_g+\sigma | J, 1, m_g, \sigma\rangle d, \quad (4)$$

where $d = er$ is the reduced dipole moment matrix element, such that the radiative decay rate of the excited state is $\Gamma = (4/3)\alpha c r^2 k^3 = d^2 k^3/3\pi\epsilon_0\hbar$. Below, we will frequently use the symbol

$$C_\pm(J,m) = \langle J+1, m_g \pm 1 | J, 1, m_g, \pm 1\rangle = \left[\frac{(J\pm m+1)(J\pm m+2)}{(2J+1)(2J+2)}\right]^{\frac{1}{2}}. \quad (5)$$

We take the Rabi frequency to be $\Omega = dE_L/\hbar$. For σ^+ laser light,

$$\begin{aligned} H_{AL} &= \hbar\Omega\cos(kz) \sum_{m=-J}^{J} C_+(J,m) \\ &\quad \times [|\, e, J+1, m+1\rangle\langle g, J, m \mid e^{-i\omega t} \\ &\quad + |\, g, J, m\rangle\langle e, J+1, m+1 \mid e^{i\omega t}] \\ &= W_{eg} e^{-i\omega t} + W_{ge} e^{i\omega t}. \end{aligned} \quad (6)$$

The on-resonance single-beam laser intensity parameter S, the detuning parameter L, and the nominal optical pumping rate Γ_p are

$$S = \frac{2\Omega^2}{\Gamma^2}, \quad L = 1 + \frac{4\delta^2}{\Gamma^2}, \quad \Gamma_p = \frac{2S\Gamma}{L}. \quad (7)$$

The recoil momentum is $P_R = \hbar k$, the recoil velocity $V_R = \hbar k/M$, and the dimensionless recoil parameter is $\epsilon = E_R/\hbar\Gamma$. Note that for a single laser beam with time average $\langle \mathbf{E}^2\rangle = E_L^2/2$, the irradiance $I = \epsilon_0 c E_L^2/2 = \pi h \Gamma c S/3\lambda^3$, using expressions given above for S, Ω, and Γ.

B. Computations with a free-particle basis

In this approach, the basis states for ρ are products of internal atomic states and free-particle momentum states:

$$|\eta, J_\eta, m, q\rangle = \psi(\eta, J_\eta, m) e^{iP_R z q/\hbar} = \psi(\eta, J_\eta, m) e^{iqkz}, \quad (8)$$

where $\eta = 0$ or g for ground states and 1 or e for excited states, and the scaled variable $q = P/P_R$.

Hamiltonian terms $H_{\rm KE}$ and H_A are diagonal in the above basis, and are given by Eq. (2) above. For example,

$$\langle \eta, J_\eta, m, q \mid H_{\rm KE} \mid \eta', J_{\eta'}, m', q'\rangle = q^2 E_R \delta(\eta,\eta')\delta(m,m')\delta(q,q'). \quad (9)$$

In view of Eq. (2) and the relation $e^{ikz} \mid q\rangle = \mid q+1\rangle$, elements of the laser interaction term H_{AL} for a σ^+ laser standing wave and a $J \to J+1$ transition are

$$\langle e, J+1, m+1, q | W_{eg} | g, J, m, q'\rangle = C_+(J,m)\frac{\hbar\Omega}{2}\delta(q, q'\pm 1). \quad (10)$$

For computational purposes, q assumes discrete values. Values of q are grouped into momentum "families" of infinite extent, such that H_{AL} connects states only within a family. Each family is labeled by Q_j:

$$q = Q_j + 2n + \eta, \quad Q_j = \frac{2j}{N}, \quad -1 < Q_j \le 1 \quad (11)$$

where j, n, and N are integers, $N > 0$. Part of one family is shown in Fig. 1(a), and for this family $q = 2n+\eta$, $N=1$, and $Q_j = j = 0$. A calculation performed with just this

family has the coarsest momentum mesh possible. Figure 1(d) shows a set of four families, with $N = 4$, $Q_j = -1/2$, 0, 1/2, and 1, to form a finer mesh.

The spontaneous decay term for any element of ρ is given by

$$\langle \eta, J_\eta, m, q \mid \dot{\rho}_{\rm SE} \mid \eta', J_{\eta'}, m', q' \rangle = -\frac{\Gamma}{2}[\eta + \eta']. \quad (12)$$

Repopulation of the ground-state elements by spontaneous decay is expressed by

$$\langle g, J, m, q \mid \dot{\rho}_{\rm repop} \mid g, J, m', q' \rangle = \Gamma \sum_{\sigma=-1}^{1} \sum_{n=0}^{N} \widetilde{\mathcal{N}}_\sigma \left(-1 + \frac{2n}{N}\right) \langle J, 1, m, \sigma | J+1, m+\sigma \rangle \times \left\langle e, J+1, m+\sigma, q-1+\frac{2n}{N} \middle| \rho \middle| e, J+1, m'+\sigma, q'-1+\frac{2n}{N} \right\rangle \times \langle J+1, m'+\sigma | J, 1, m', \sigma \rangle. \quad (13)$$

$\widetilde{\mathcal{N}}_\sigma(r)$ is a discretized version of the functions for angular distribution of emitted fluorescence, namely, $\mathcal{N}_{\pm 1}(r) = \frac{3}{8}(1 + r^2)$ and $\mathcal{N}_0(r) = \frac{3}{4}(1 - r^2)$, where $-1 \le r \le 1$. For a numerical mesh of $2P_R/N$, we divide the interval $-1 \le r \le 1$ into $N + 1$ equal segments, and obtain

$$\widetilde{\mathcal{N}}_\sigma \left(-1 + \frac{2n}{N}\right) = \int_{a(n)}^{b(n)} \mathcal{N}_\sigma(y)dy, \quad n = 0, 1, \ldots, N \quad (14)$$

where $a(n) = -1 + 2n/(N + 1)$ and $b(n) = -1 + 2(n + 1)/(N + 1)$. This discretization is somewhat arbitrary, but gives the correct distribution as $N \to \infty$. It is shown schematically in Fig. 1(b) for $N = 1$ and in Fig. 1(e) for $N = 4$. Figures 1(c) and 1(f) show the relative intensities of spontaneous decay for various ΔP in the two cases.

To compute the time evolution of ρ, matrix elements of ρ are arranged in a vector X. The Hamiltonian and decay terms provide the evolution matrix T, such that

$$\dot{X} = TX. \quad (15)$$

After computing $\rho(t)$ by the above method, it is sometimes of interest to obtain the spatial distribution $P(z, t)$. From Eq. (8),

$$P(z,t) = \sum_{q,q',\eta,\eta',m,m'} e^{ikz(q-q')} \times \langle \eta', J_{\eta'}, m', q' | \rho | \eta, J_\eta, m, q \rangle. \quad (16)$$

C. Methods for numerical optimization

In view of the Hermitian symmetry of $\rho = \rho^\dagger$, the number of stored elements can be reduced. We need only the elements in the upper triangle of $\mathrm{Im}(\rho)$ and the upper triangle plus diagonal elements in $\mathrm{Re}(\rho)$. We use IMSL computer subroutine DIVPAG or NAG subroutine D02BAF for the time integration, both of which require real variables.

When $-n_{\max} \le n \le n_{\max}$, there are $2n_{\max} + 1$ basis states for each atomic sublevel. We have used $n_{\max}$ as large as 750, implying 3002 basis states for a two-level calculation. This would mean in principle 9×10^6 elements in ρ and 8×10^{13} elements in T. The free-particle approach becomes practical only because most of these elements are negligible. For example, since only basis states within families are connected by H_{AL}, only off-diagonal elements between states *within* each family need be retained. Spontaneous emission connects different families

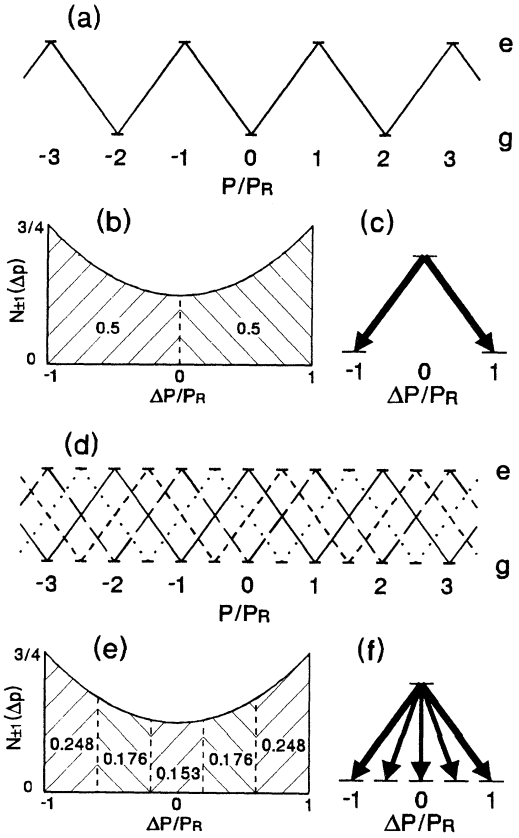

FIG. 1. Families and discretized spontaneous emission in free-particle basis calculations. (a), (b), and (c) are for a single family in a two-level transition, showing basis states connected by the atom-laser interaction. For $\sigma^\pm$ emission, the spontaneous decay is equally split between $\Delta P = \pm P_R$. (d) shows a finite part of four families, spaced by $P_R/2$, while (e) and (f) show the probabilities of various ΔP values discretized over the range $-1 \le \Delta P \le 1$.

but does not induce coherences.

Furthermore, since off-diagonal elements with $|q-q'| = |\Delta q|$ arise from laser interactions of order $|\Delta q|$, for a given intensity and detuning, values of $|\Delta q| > |\Delta q|_{\text{cutoff}}$ may be neglected. $|\Delta q|_{\text{cutoff}}$ can be determined by trial and error by comparing the calculated results for $P(V,t)$ as shown in Sec. III F below. $|\Delta q|_{\text{cutoff}}$ is often in the range 4–8, and not more than 20 in any calculation performed in this work. Hence the required number of off-diagonal elements with the free-particle basis is considerably less than $\mathfrak{N}^2$. In addition, the evolution matrix T is extremely sparse. The maximum number of elements in each row in two-level cooling calculations is $6 + 2|\Delta q|_{\text{cutoff}}$, so a calculation that requires 50 000 elements in ρ will have only 10–50 elements in each row of T.

With these numerical optimizations and the use of computers with larger memory, we are able to use a finer mesh and a larger range of momenta than in previous work with the free-particle approach. Because of the relatively few off-diagonal elements required, the method scales as $\mathfrak{N}$ rather than $\mathfrak{N}^2$, hence is competitive with Monte Carlo methods applied to the Schrödinger equation.

D. Method of the periodic potential

When the excitation is weak, $S/L \ll 1$, excited-state elements can be eliminated from the density matrix equations. The effective Hamiltonian for the ground state then includes a periodic light-shift potential matrix [8,20]. This matrix is diagonal for $\sigma^{\pm} - \sigma^{\pm}$ laser polarization, giving a Mathieu equation for each m. In all cases for which we have used the periodic potential basis, only diagonal elements of ρ have been required (secular approximation), hence the dimension of the calculation can be enormously reduced relative to the free-particle basis approach. The price to be paid is that Doppler cooling processes are not included (because the excited state is eliminated).

To derive equations for the ground state in the presence of the periodic potential, we write the Liouville equation for the full density matrix. We take W_{eg} and W_{ge} from Eq. (6) and use the notation $\rho_{gg'}$ to mean $\langle g, J_g, m_g, p \mid \rho \mid g, J_g, m_g', p' \rangle$. We obtain

$$i\hbar\dot{\rho}_{gg'} = \frac{p^2 - p'^2}{2M}\rho_{gg'} + \sum_{e''}\{W_{ge''}s_{e''g'} - s_{ge''}W_{e''g'}\} + i\hbar\dot{\rho}_{\text{repop}}, \quad (17)$$

$$i\hbar\dot{\rho}_{ee'} = \frac{p^2 - p'^2}{2M}\rho_{ee'} + \sum_{g''}\{W_{eg''}s_{g''e'} - s_{eg''}W_{g''e'}\} - i\hbar\Gamma\rho_{ee'}, \quad (18)$$

$$i\hbar\dot{s}_{ge'} = \frac{p^2 - p'^2}{2M}s_{ge'} + \hbar\delta s_{ge'} + \sum_{e''}\{W_{ge''}\rho_{e''e'} - \rho_{gg''}W_{g''e'}\} - i\hbar\frac{\Gamma}{2}s_{ge'}. \quad (19)$$

Coherences between ground and excited states have been rewritten using the substitution $\rho_{ge'} = s_{ge'}e^{i\omega t}$.

We now assume that the kinetic energy terms in Eqs. (18) and (19) are negligible. This is equivalent to neglecting the Doppler shift, i.e., we assume $kv \ll \Gamma$ (cf. [9]). Although Doppler cooling is not present, the effects discussed in Sec. IV are unaffected since they arise from the non-Doppler process of $\Delta m = 1$ excitation and spontaneous decay as shown for a $J = 1/2 \rightarrow 3/2$ transition in Fig. 2(a). When the Doppler shift *is* included using the free-particle method, these transient features are superposed on a broad Doppler cooling "background" peak.

In the low excitation regime ($S/L \ll 1$), $\rho_{ee'}$ may be neglected relative to $\rho_{gg'}$. Furthermore, we adiabatically eliminate the excited-state elements and ground-excited state coherences (cf. [8]) by setting $\dot{\rho}_{ee'} = 0$ and $\dot{s}_{ge'} = 0$ in Eqs. (18) and (19), and solve these equations to obtain expressions for $\rho_{ee'}$ and $s_{ge'}$ in terms of $\rho_{gg'}$. Then we substitute these expressions into Eq. (17), to obtain the time evolution of the ground-state density matrix elements alone, $\tilde{\rho}_{gg'}$. Our notation is made compact by defining a Clebsch-Gordan matrix, $C^{\sigma}_{eg} = \langle J+1, m+\sigma | J, 1, m, \sigma \rangle$, and a matrix operator R that expresses the process of laser excitation and spontaneous decay with polarization σ and with recoil:

$$R^{\sigma}_{g',g}(q) = \sum_{e} W_{g'e}C^{\sigma}_{eg}e^{iqkz}. \quad (20)$$

We also use the abbreviation $\sum_e W_{ge}W_{eg'} = A_{gg'}$. Finally, the resulting equation for the time evolution of the ground-state matrix elements alone is

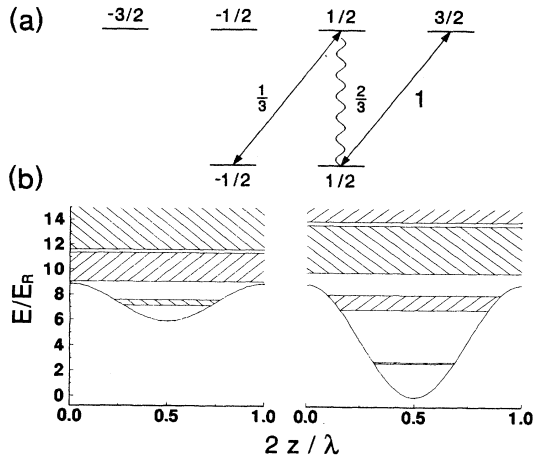

FIG. 2. (a) Excitation scheme for σ^+ laser light on a $J = 1/2 \rightarrow 3/2$ transition. Solid arrows denote transitions on which Doppler cooling occurs. Spontaneous decay, indicated by the wavy arrow, introduces a non-Doppler process. (b) One period of the periodic light-shift potentials for $m_g = -1/2$ (left) and $m_g = 1/2$ (right). Allowed energy bands are shaded. The difference in well depth arises from the Clebsch-Gordan factors shown in (a). Band gaps are large within the potential wells but become narrow just above the wells.

$$i\hbar\dot{\tilde{\rho}} = \frac{1}{2M}[\hat{P}^2, \tilde{\rho}] + \frac{4\delta}{\hbar\Gamma^2 L}[A, \tilde{\rho}] - \frac{2i\Gamma}{\hbar\Gamma^2 L}\{A, \tilde{\rho}\}_+ + \frac{i\hbar\Gamma}{L}\sum_{\sigma=-1}^{1}\int_{-1}^{1} dq N_\sigma(q) R^\sigma(q)^\dagger \tilde{\rho} R^\sigma(q). \quad (21)$$

In analogy with Eq. (1), we interpret $\hat{P}^2/2M - 4\delta A/\hbar\Gamma^2 L$ as the effective Hamiltonian H_{eff} for the ground-state density matrix. The third term depletes the ground-state populations; the fourth term feeds them (cf. [20]).

The operator A is given by (from now on, $J \equiv J_g, m \equiv m_g$)

$$A = \hbar^2\Omega^2 \sum_m C_+(J,m)^2 \cos^2(kz) \mid m\rangle\langle m \mid, \quad (22)$$

which is diagonal in m. The operator $\cos^2(kz)$ over the momentum basis can be written $\int_{-\infty}^{\infty} dp\{\frac{1}{2}|p\rangle\langle p| + \frac{1}{4}[|p\rangle\langle p - 2\hbar k| + |p\rangle\langle p + 2\hbar k|]\}$. The Schrödinger equation $H_{\text{eff}}\Psi = E\Psi$ involves $2J+1$ independent differential equations, each associated with a single ground-state magnetic quantum number m:

$$\left(\frac{\hat{P}^2}{2M} + \frac{4\hbar\Omega^2\delta}{\Gamma^2 L} C_+(J,m)^2 \cos^2(kz)\right)\psi = E\psi. \quad (23)$$

In a position representation, we have a Mathieu equation [41,42] for each channel:

$$\frac{d^2\psi}{d\zeta^2} + \left[\lambda + \frac{u(m)}{2}\cos(2\zeta)\right]\psi = 0, \quad (24)$$

where

$$u(m) = C_+(J,m)^2 \frac{U_0}{E_R}, \quad U_0 = -\frac{2S\hbar\delta}{L}, \quad \lambda = \frac{E}{E_R} + \frac{u(m)}{2} \quad (25)$$

and we have substituted $kz = \zeta$. Solutions to these Mathieu equations have the general form

$$\psi(m,n,\nu;\zeta) = \sum_{j=-\infty}^{\infty} a_j(m,n,\nu) e^{i(2j+\nu)\zeta}. \quad (26)$$

This wave function satisfies Floquet's theorem with a period π and Bloch-Floquet index ν: $\psi(m,n,\nu;\zeta+\pi) = e^{i\nu\pi}\psi(m,n,\nu;\zeta)$. In solid state physics, ν is often called a quasimomentum [43]. As is well known [41], the stable (nondivergent) solutions of the Mathieu equation occur in energy bands, denoted n here, alternating with band gaps of forbidden energies. Below the tops of periodic potential wells, that is, for $E < U_0$, the bands are narrow, while for $E > U_0$, the gaps are narrow, as shown for a few levels in Fig. 2(b). $\psi(m_g,n,\nu;\zeta)$ can be interpreted as a wave function in coordinate space and a_j a vector of coefficients over the momentum functions. By inserting this solution into Eq. (24), we obtain recursion relations that determine the coefficients a_j (for numercal calculations, a suitable cutoff is made) and eigenvalues. Once the coefficients a_j are found, we may evaluate Eq. (21) over the periodic potential basis using sums over the a_j.

The temporal evolution given by Eq. (21) then assumes the form $\dot{\tilde{\rho}} = \widetilde{T}\tilde{\rho}$, and again the elements of $\tilde{\rho}$ may be placed in a vector, such that $\widetilde{T}$ is the Liouville matrix for the ground state. Since only ground-state diagonal density matrix elements are needed, these calculations require much less memory, are much faster than free-particle basis calculations, and can often be performed on a 486 PC. No elaborate numerical optimization schemes were needed.

E. Semiclassical theory of laser cooling

Following earlier discussions [12,13,15], Berg-Sørensen *et al.* [17] have recently presented a particularly clear and useful derivation of the force and diffusion parameters for two-level Doppler cooling for use in a Fokker-Planck equation (FPE). We will briefly summarize their results in the notation used in the present work. Their derivation, like others, is based on the Wigner matrix:

$$W_{\alpha,\beta}(z,P,t) = \frac{1}{h}\int_{-\infty}^{\infty} du\, e^{(-iPu/\hbar)} \times \left\langle z + \frac{u}{2}\middle|\rho_{\alpha,\beta}\middle| z - \frac{u}{2}\right\rangle, \quad (27)$$

where $\alpha,\beta = e,g$ and $\rho_{\alpha,\beta}$ solves the optical Bloch equations. Moments of the Wigner matrix,

$$W^n(t) = \int_{-\infty}^{\infty} dz \int_{-\infty}^{\infty} dP P^n W(z,P,t), \quad (28)$$

in view of the relation $\langle P^n\rangle(t) = \mathrm{Tr}W^n(t)$, lead to the force and diffusion functions:

$$F = \frac{d\langle P\rangle}{dt}, \quad D = \frac{1}{2}\frac{d}{dt}\left(\langle P^2\rangle - \langle P\rangle^2\right). \quad (29)$$

Also it is useful to define

$$\widetilde{W}^1 = W^1 - (\mathrm{Tr}W^1)W^0 = \int dP(P - \langle P\rangle)W(P,t) \quad (30)$$

such that $\mathrm{Tr}(\widetilde{W}^1) = 0$.

Since $\mathrm{Tr}(W^0) = 1$, Bloch equations for $W(z,P,t)$ are most easily expressed in terms of the components $W^0_- = W^0_{gg} - W^0_{ee}, W^0_R = \mathrm{Re}W^0_{eg}$, and $W^0_I = \mathrm{Im}W^0_{eg}$. In semiclassical theory, d/dt in the Bloch equations for $W(z,P,t)$ is replaced by Vd/dz, as if the atom were dragged through the laser field at constant velocity, $z = Vt$. (Consequences of this assumption will be evident in the following section.) Bloch equations for $W^0_-, W^0_R, W^0_I, \widetilde{W}^1_-, \widetilde{W}^1_R$, and $\widetilde{W}^1_I$ are given in Eqs. (2.29) and (2.30) of Ref. [17]. Each of these elements $w = W^0_-$ etc. is expanded in a Fourier series

$$w = \sum_n e^{inkz} w_n \quad (31)$$

and solutions obtained by matrix continued fraction techniques (Ref. [17]). For the FPE, one needs spatially averaged force and diffusion coefficients and these are [Eqs. (A.9) of [17]]

$$\bar{F} = 2\hbar k\Omega \ \mathrm{Im}(W_R^0)_1, \tag{32}$$

$$\bar{D} = \frac{1}{4}(\hbar k)^2\Gamma\left[\frac{8\Omega}{\hbar k\Gamma}\ \mathrm{Im}(\widetilde{W}_R^1)_1 + \frac{2}{5}[1-(W_-^0)_0]\right]. \tag{33}$$

These parameters are then inserted into a FPE of the form

$$\frac{\partial w}{\partial t} = -\frac{\partial}{\partial P}(\bar{F}w) + \frac{\partial}{\partial P}\left(\bar{D}\frac{\partial w}{\partial P}\right). \tag{34}$$

This particular form of the second term on the right was found to be most accurate [17] (see also Ref. [44]). Furthermore, by setting $\partial w/\partial t = 0$, the steady-state momentum distribution is obtained:

$$w(P, t=\infty) = \exp\left(\int_{-\infty}^{P} dP'\bar{F}(P')/\bar{D}(P')\right). \tag{35}$$

Results obtained with the above method are compared with results from quantum density matrix calculations for many of the conditions considered in Sec. III.

To place our discussion of anomalous effects into context, we will briefly summarize and refine semiclassical theory for near-optimum, low intensity Doppler cooling for small ϵ, which for several years was a primary concern of laser cooling theory. In this model theory, force is considered only to first order in velocity, and diffusion is assumed to be velocity independent. We will repeat previous expressions for $F(z,V)$ and $D(z)$, then perform a spatial average of each to obtain a Maxwell (thermal) distribution in V. The derived temperature as a function of laser intensity and detuning is valid when the linearized expressions are valid. The $F(z,V)$ function itself will be of interest in Sec. III C because it yields classical trajectories with dissipation and without spatial averaging over the light-shift potential wells. From optical Bloch equations, using a saturation parameter we label $s = (4S/L)\cos^2(kz)$, Gordon and Ashkin [12] obtained

$$F(z,V) = \frac{\hbar k s\delta \tan(kz)}{1+s} \times\left[1 + \frac{4(1-s)-2s^2L}{L\Gamma(1+s)^2}Vk\tan(kz)\right] \tag{36}$$

and

$$D(z) = \frac{(\hbar k)^2\Gamma s\tan^2(kz)}{4(1+s)^3}\left[Ls^3+3s^2+\frac{s}{3}(4-L)+1\right] + \frac{2}{5}\frac{s}{1+s} \tag{37}$$

[see also Eq. (2.31) of Ref. [17]].

In our notation, with $s_0 = 4S/L$, the spatial average of the linear coefficient of velocity in $F(z,V)$ (damping coefficient) is [45]

$$\bar{F}_1 = \frac{\hbar k^2 2\delta}{\Gamma(1+s_0)^{3/2}} \times\left[\frac{s_0}{L}\left(1+\frac{s_0}{2}\right) - 1 - \frac{3}{2}s_0 - \frac{3}{8}s_0^2 + (1+s_0)^{3/2}\right] \tag{38}$$

while the spatial average of velocity-independent $D(z)$ (not derived previously to our knowledge) is

$$\bar{D}_0 = \frac{(\hbar k)^2\Gamma}{32(1+s_0)^{3/2}} \times\left\{(1+s_0)^{3/2}\left[4s_0L + 24(L-1) + \frac{16}{5}\right] + (24+40s_0)(1-L) + s_0^2\left(\frac{4}{L}+11-15L\right) - \frac{16}{5}(1+s_0)\right\}. \tag{39}$$

When the force curve is linear with velocity over the steady-state velocity distribution, that distribution is Gaussian, and a temperature may be defined:

$$k_BT = \frac{\bar{D}_0}{\bar{F}_1}. \tag{40}$$

When the distribution is Gaussian, the usual relationship for one dimension, $k_BT/2 = MV_{\mathrm{rms}}^2/2 = \bar{E}_K$, applies. To order s_0^3 in $\bar{F}_1$ and in $\bar{D}_0$,

$$k_BT = \frac{7\hbar\Gamma^2}{80}\frac{L}{|\delta|}\left[1+\frac{5s_0}{7}\left(\frac{1}{L}+\frac{9}{10}\right) - \frac{7}{16}s_0^2 + \cdots\right]. \tag{41}$$

Hence the minimum Doppler cooling temperature found by this reasoning is

$$k_BT_{\min} \overset{s_0\to 0}{\longrightarrow} \frac{7\hbar\Gamma}{20}, \quad \delta = -\frac{\Gamma}{2}. \tag{42}$$

This result agrees with Aspect *et al.* [7] and is confirmed to high precision by quantum calculations. If the interest is solely in the minimum Doppler cooling temperature, Eq. (42) concludes the discussion.

From full SC and QDM calculations, Eq. (41) is found to be a good approximation for $S/L \ll 1$. At higher intensities, nonlinear terms in $\bar{F}$ and $\bar{D}$ become important, and $P(V,t)$ becomes non-Gaussian. One could plot temperature, or even $\langle E_K\rangle$ for a non-Gaussian distribution, as a function of intensity and detuning from Eqs. (41) or (38)–(40) as compared with full SC or QDM calculations. In the following discussion, however, the focus will be on the physical processes that underlie distinctive features in $P(V,t)$ rather than on $\langle E_K\rangle$ or k_BT.

In connection with the discussion of Doppleron features in Sec. III D, it is of interest to have a formula for the velocities at which Doppleron peaks occur in the force curve, including effects of laser intensity. The zeroth-order expression, given in the Introduction, will be seen to be quite inaccurate. Kyrölä and Stenholm [38] considered the jth Doppleron resonances using a continued fraction expression for the force. The following equations are obtained from their derivation, using our parameters defined in Sec. II A. However, we find that our calculated Doppleron peaks at high laser intensity require additional terms in the expansion, or alternatively, the square root factors as given below:

$$kV_{\mathrm{res}} = \begin{cases} \delta\left[1+\frac{S\Gamma^2}{4\delta^2}\right]^{1/2}, & j=0\,, \\ \frac{\delta}{2j+1}\left[1+\frac{(2j+1)S\Gamma^2}{4j\delta^2}\right]^{1/2}, & j>0\,. \end{cases} \tag{43, 44}$$

III. TIME EVOLUTION OF THE VELOCITY DISTRIBUTION IN TWO-LEVEL DOPPLER COOLING

In this section, we present figures showing the time evolution of the velocity distribution $P(V,t)$ in two-level Doppler cooling. We find that there is a remarkable degree of structure in $P(V,t)$ from various processes, some of which have not been recognized previously. Also, it is notable that there is generally excellent agreement between results obtained from the free-particle quantum density matrix approach and from the semiclassical Fokker-Planck equation. The exceptions to this are the regime near $V = 0$, where light-shift potential well effects enter in the QDM results but not the SC results, and the regime of large recoil energies, where the assumptions of the FPE are violated.

A. Optimum Doppler cooling

We first present results for optimum laser parameters to compare with other conditions. The minimum temperature for two-level Doppler cooling is obtained with $\delta = -\Gamma/2$ and low intensity [see Eqs. (41) and (42)]. The semiclassical force function with this detuning has peaks at approximately $kV = \pm\Gamma/2$, as shown in Fig. 3(a) for $S = 0.2$. Figures 3(b) and 3(c) show calculated velocity distributions as a function of time for $\delta = -\Gamma/2, S = 0.2$, and ϵ =0.0025, as for a two-level atom with mass and resonance wavelength equal to that of sodium atoms cooled on the D_2 line (see Table I). For this calculation, the initial velocity distribution $P(V,0)$ was flat up to $|V| = 280V_R$. For both SC and QDM, the last three traces in Fig. 3(c) coincide, showing convergence. The SC results converge to the SC steady-state distribution.

The short-term time evolution obtained from QDM calculations in Fig. 3(b) exhibits a dip at $V = 0$ and clearly departs from Gaussian form. The long-term QDM results also exhibit a deficiency of atoms near $V = 0$ relative to SC results, but less dramatically. As discussed in more detail below, the range of these effects is approximately $E_K = (V/V_R)^2 E_R \leq U_0$. The well depth U_0 [Eq. (25)] of $40E_R$ corresponds to $V \approx 6.3V_R$ here.

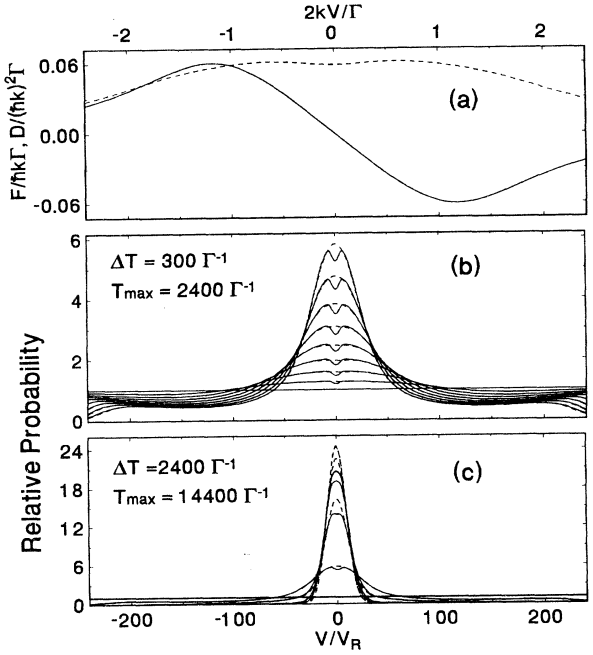

FIG. 3. "Optimum" Doppler cooling with $\delta = -\Gamma/2, S = 0.2$, for a two-level atom with $\epsilon = E_R/\hbar\Gamma = 0.0025$, as for sodium cooled on the D_2 line, hence $U_0 = 40E_R$. (a) Semiclassical force (solid line) and diffusion (dashed line) functions; (b) $P(V,t)$ for short times; (c) $P(V,t)$ for longer times. In (b) and (c), solid lines denote QDM results and dashed lines denote SC results for a succession of interaction times as indicated. The horizontal scales of (a), (b), and (c) are the same.

The semiclassical force function scales as kV/Γ and is independent of E_R. For optimum cooling, $MV_{\rm rms}^2/2 \approx \hbar\Gamma$ and thus $V_{\rm rms}$ varies as $M^{-1/2}$. Thus in units of Γ/k the width of the central peak in the velocity distribution increases as E_R increases. Figure 4 shows a calculation similar to that in Fig. 3 but for $\epsilon = 0.0266$, as for a two-level atom with the mass and wavelength of helium cooled on the $2\,^3S \rightarrow 2\,^3P$ transition at 1.08 μm. The differences with semiclassical results in this region are greater, and the long-term QDM result shows a comparable departure from SC calculations. For the calculations of Fig. 4, $U_0 =$

TABLE I. Parameters for some atomic transitions of interest in this work, ordered by $E_R/\hbar\Gamma$.

Atom	Transition	λ (nm)	$\Gamma/2\pi$ (MHz)	E_R/h (kHz)	$E_R/\hbar\Gamma$
Cs	$6\,^2S \rightarrow 6\,^2P_{3/2}$	852	5.30	2.07	3.90×10^{-4}
Rb	$5\,^2S \rightarrow 5\,^2P_{3/2}$	780	5.96	3.86	6.43×10^{-4}
Na	$3\,^2S \rightarrow 3\,^2P_{3/2}$	589	9.72	25.01	2.57×10^{-3}
Cr	$a\,^7S_3 \rightarrow z\,^7P_4$	425	5.0	21.2	4.24×10^{-3}
Li	$2\,^2S \rightarrow 2\,^2P$	671	5.87	63.18	1.08×10^{-2}
He	$2\,^3S_1 \rightarrow 2\,^3P_2$	1083	1.63	42.46	2.61×10^{-2}
H	$1\,^2S \rightarrow 2\,^2P$	122	99.5	1.34×10^4	0.13
He	$2\,^3S_1 \rightarrow 3\,^3P_2$	389	1.6	330	0.21
Sr	$5\,^1S \rightarrow 5\,^3P_0$	689	7.58×10^{-3}	4.8	0.63
Ca	$4\,^1S \rightarrow 4\,^3P_0$	657	3.2×10^{-4}	11.6	36.4

$3.8E_R$, and correspondingly, the appreciable deviations between QDM and SC results are in the range $|V| < 2V_R$.

B. Larger than optimum detuning or intensity

We will discuss several processes which give rise to a transient dip in $P(V,t)$ at $V = 0$. Perhaps the most obvious is simply larger than optimum detuning. In the approximation of linear $F(P)/D(P)$, the steady-state distribution broadens with detuning as seen from Eq. (35) and as discussed by Lett *et al.* [5]. However, the temporal evolution of the velocity distribution is quite different with larger detuning than with $\delta \approx -\Gamma/2$. The reasons are evident upon considering the semiclassical force function. Figure 5 shows the situation for $\delta = -3\Gamma$, $S = 1.0$, $\epsilon = 0.0266$, and $U_0 = 6.1E_R$. The SC force function [Fig. 5(a)] near $V = 0$ exhibits smaller slope than with $\delta \approx -\Gamma/2$, so atoms near $V = 0$ are cooled more slowly. Because of the pronounced peaks in $F(V)$ at $V = \pm(3/2)\Gamma/k$, atoms are collected at velocities just within $V = \pm(3/2)\Gamma/k$ and migrate slowly toward $V = 0$. The broad dip in $P(V,t)$ at $V = 0$ can persist for a relatively long time, as shown in Figs. 5(b) and 5(c). Eventually $P(V,t)$ assumes a near-Gaussian form, although again QDM results exhibit fewer atoms near $V = 0$ than the SC calculation.

At high laser intensity, $P(V,t)$ becomes noticeably non-Gaussian even in the steady-state limit. Examples of optimum detuning but high intensity are shown in Fig. 6. For this figure, $\delta = -\Gamma/2$, $S = 10.0$, and $\epsilon = 0.0266$ ($U_0 = 188E_R$) in Fig. 6(b) and 0.0025 ($U_0 = 2000E_R$) in Fig. 6(c). These results will be discussed in the following subsection.

C. Effect of slower cooling in the light-shift potential wells

The deficiency of atoms near $V = 0$ in the QDM results relative to SC results in Figs. 3, 4, and 6 is not from detuning, but due to a deficit of very slow atoms caused by slower cooling in the wells. This effect has been observed in experiments on helium atoms, as reported in Ref. [23]. It is not seen in SC results because the force function, as shown in Figs. 3(a), 4(a), and 5(a), is obtained by averaging over a spatial period. Bigelow and Prentiss [34] used the spatially varying force function $F(z,V)$ obtained by Gordon and Ashkin [our Eq. (36)] in classical trajectory calculations to show that the cooling rate dE_K/dt for atoms with $E_K < U_0$ is slower than for atoms with $E_K > U_0$. For $E_K > U_0$, there is some modulation of velocity as the atom passes periodically over the potential maxima, while for $E_K < U_0$, an atom will oscillate in one of the wells. When averaged over a period of motion, $\langle V^2 \rangle$ decreases more rapidly for $E_K > U_0$, for which Doppler cooling operates more efficiently, than for $E_K < U_0$ [34].

In quantum calculations, the transient dip in $P(V,t)$ at $V = 0$ due to a deficiency of atoms in the wells is a ubiquitous feature. Such a dip appears in Fig. 7(a) in the

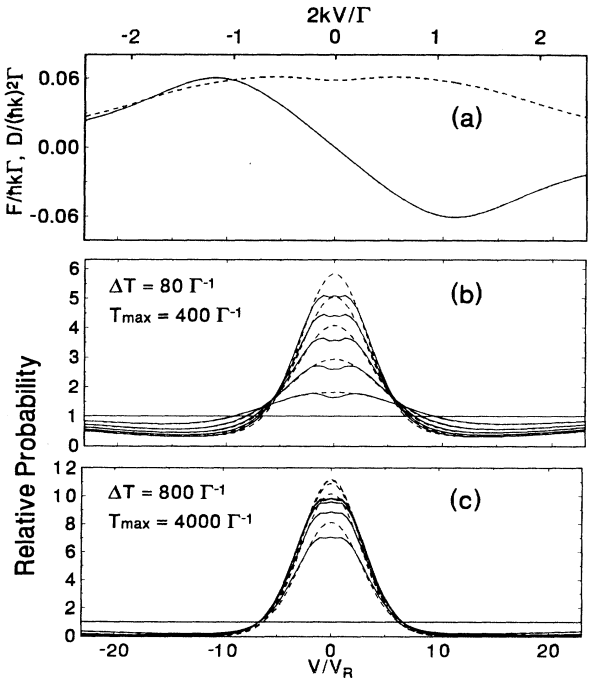

FIG. 4. SC and QDM results for "optimum" Doppler cooling with δ and S as in Fig. 2 but for a two-level atom with $\epsilon = 0.0266$, as for helium cooled on the $2\,^3S \rightarrow 2\,^3P$ (1.08 μm) transition, and thus $U_0 = 3.8E_R$. In units of $2kV/\Gamma$, the horizontal scale and hence the force curve is the same as in Fig. 2, but in units of V_R there is a difference of about a factor of 10.

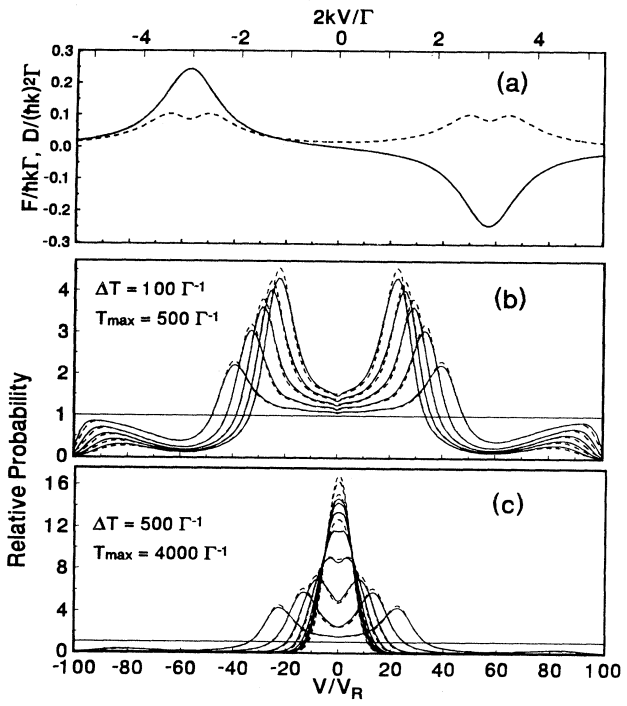

FIG. 5. Doppler cooling of a two-level atom with larger than optimum detuning. Here $\delta = -3\Gamma, S = 1$, $\epsilon = 0.0266$ (He*), and $U_0 = 6.1E_R$. A broad dip at $V = 0$ persists for many Γ^{-1}, but eventually the velocity distribution becomes Gaussian. Solid and dashed lines have the same meaning as in Fig. 3.

region $|V/V_R| < 3$, together with a wider dip from the $\delta = -2\Gamma$ detuning as discussed for Fig. 5. Figure 7(b) shows the populations of the lowest quantum states in the light-shift potential, projected from the free-particle basis results. The lowest states are underpopulated for a time, and then nearly catch up to the populations of states at the top of the potential (E=0). When the detuning is sufficiently large that the optical pumping rate is less than the oscillation frequency for atoms in the well, $\Gamma_p < \omega_v = 2\sqrt{(U_0 E_R)}/\hbar$, an atom can oscillate in one of the light-shift potential wells before it is excited, hence the dip is more sharply defined. This is shown in Figs. 8(a) and 8(b), for which $\Gamma_p/\omega_v = 0.25$ and 0.45, respectively. The vertical dashed lines in Fig. 8 denote the threshold velocity values V_0 for which $MV_0^2/2 = U_0$. The well effects extend to about $V = 0.9V_0$ in these cases.

When the excitation rate Γ_p is more rapid than the oscillation frequency ω_v, well effects and differences between SC and QDM results are found only for atoms relatively deep in the wells ($E_K \ll U_0$ or $V < V_0$). This is seen in Figs. 6(b) and 6(c), for which $\Gamma_p/\omega_v = 13.6$ and 34.6, respectively. In Fig. 6(b), $P(V, t = \infty)$ is quite flat up to $V = \pm 8V_R$, as compared with $V_0 \approx 14V_R$. In Fig. 6(c), the dip at $V = 0$ extends to approximately $V = \pm 25V_R$, as compared with $V_0 \approx 45V_R$. So for Figs. 6(b) and 6(c), well effects extend to about $V = 0.5V_0$.

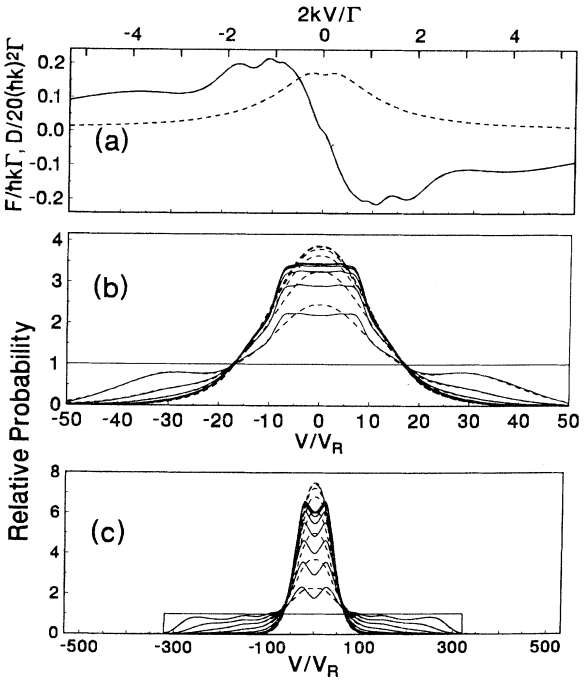

FIG. 6. Results for high intensity, low detuning. Here S=10 and $\delta = -\Gamma/2$. (a) Force (solid line) and diffusion (dashed line) functions. (b) Evolution of the velocity distribution for $\epsilon = 0.0266$ (He*), with $U_0 = 188E_R$. (c) The same for $\epsilon = 0.0025$ (Na), with $U_0 = 2000E_R$. Spatial averaging removes the effects of the light-shift wells in the SC results (dashed lines) but this is not the case for QDM results (solid lines). In (c), the initial velocity distribution was flat to $|V| = 320V_R$.

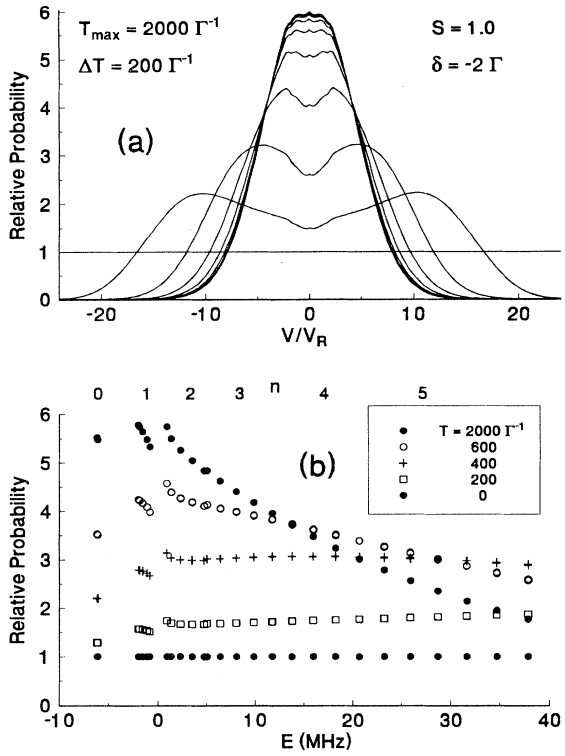

FIG. 7. Dips at $V = 0$, for $\epsilon = 0.0266$ (He*) with $U_0 = 4.4E_R$. (a) The broad transient dip is due to the -2Γ detuning, while the narrower dip is due to a slower cooling rate for atoms in the potential wells. (b) The population of quantum states below the tops of the periodic potential ($E = 0$) lags behind the populations of states above $E = 0$.

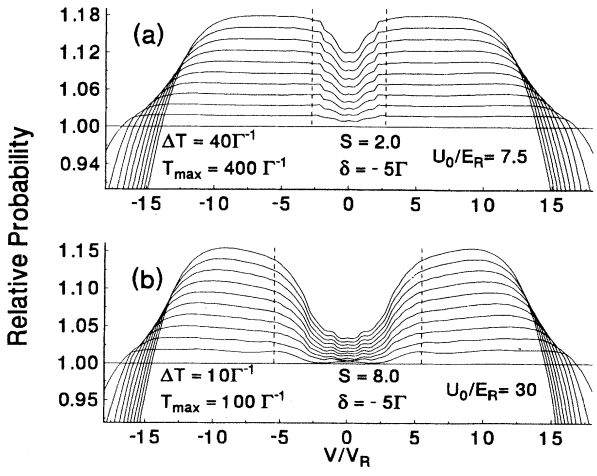

FIG. 8. Closeup views of transient dips at $V = 0$ due to slower cooling in the potential wells, for $\epsilon = 0.0266$ and for relatively short interaction times as indicated. The vertical dashed lines denote the velocities for which $MV^2/2 = U_0$, and show that the width of the dip is correlated with the depth of the potential.

These deviations between SC and QDM results near $V = 0$ reflect the breakdown of the assumption of constant V (the "dragged atom") discussed below Eq. (30), and the failure of spatial averaging used to obtain $\bar{F}$ and $\bar{D}$ for the FPE. This leads to the related question of localization of atoms in the laser standing wave, which has previously been considered in Ref. [9] for lin $\perp$ lin cooling, and also in Ref. [16], regarding non-Gaussian velocity distributions in model 3D and 1D calculations. In Ref. [9], an integral equation approach was derived to replace the FPE in this regime, while Ref. [16] used a Langevin equation with spatially varying force. From QDM results, $P(z,t)$ can be computed from Eq. (16).

It is interesting to compare QDM localization results with an estimate based on Eq. (41) and the assumption of a Maxwellian thermal velocity distribution over the periodic potential. One then has $P(V,z) = N_M \exp\{-[MV^2/2 + U(z)]/k_BT\}$, where N_M is a normalization factor, $U(z) = -U_0 \cos^2(kz)$, and k_BT is given by Eq. (41). The spatial distribution is $P(z) = \bar{N}_M \exp[-U(z)/k_BT]$, where $\bar{N}_M$ is a new normalization factor. We define a "localization ratio" $R_L = P(z = 0)/P(z = \lambda/4)$, which equals $\exp(U_0/k_BT)$ for such a thermal distribution. $R_L > 1$ corresponds to localization in the wells (antinodes for red detuning). R_L increases as S/L increases. Since Eq. (41) becomes increasingly invalid as S/L increases beyond 0.1, here we consider simply $S/L = 1/8$, for which the ratio U_0/k_BT attains the value 0.55 at large detuning, giving $R_L = 1.73$. In contrast, the largest value of R_L we obtain from QDM calculations and Eq. (16) is 1.22, for $S = 1, \delta = -\Gamma(S/L = 0.2)$. We find that R_L is essentially independent of ϵ, at least over the range $0.0025 < \epsilon < 0.027$.

Typical results for $P(z,t)$ are shown in Fig. 9. The conditions are the same as for Fig. 7, and a comparison of the two figures indicates that the dip at $V = 0$ in $P(V,t)$ persists even when there is some degree of localization in the wells. The value of R_L obtained at the longest interaction time here is 1.17, which is slightly less than the global maximum of 1.22, and much less than the thermal value of 1.66 for this S and δ. For short interaction times, Fig. 9 shows that there is a small degree of localization at the nodes rather than at the antinodes. This is consistent with evidence presented above that cooling into the wells is slower than cooling of free atoms, and with the comment in Ref. [16] that a degree of localization at the nodes occurs because (in the weak excitation limit) atoms move more slowly over the potential maxima, hence spend more time there. For longer times, Fig. 9 shows that this effect becomes less important than the accumulation of atoms in states of localized motion in the wells. For a model cooling problem in Ref. [16], there was found to be localization at the nodes in the steady-state solution. Our results do not indicate such an extreme departure from a thermal distribution, but clearly the population in the wells is significantly less than thermal. This conclusion is another indication that atoms in the wells are not cooled as efficiently as atoms with $E_K > U_0$.

It seems unlikely that the deviations between SC and QDM results near $V = 0$ are truly "quantum" effects, or that the quantum levels themselves play a significant role. It is more probable that the QDM method is simply a convenient method to take into account spatial variation in velocity. Other SC approaches that avoid spatial averaging, such as the integral equation method of Ref. [9] or the Langevin equation method of Ref. [16], may be capable of reproducing the well effects obtained with QDM, but to our knowledge this has not yet been demonstrated quantitatively for two-level Doppler cooling.

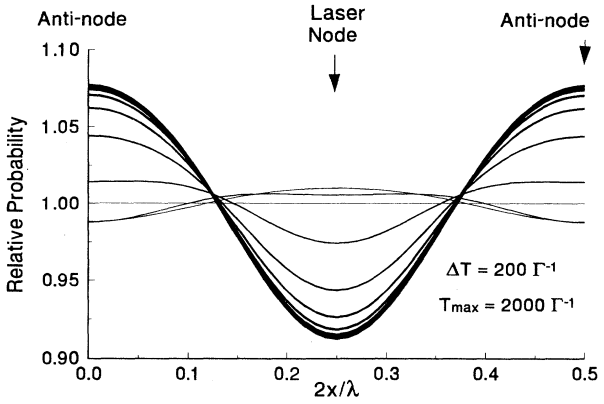

FIG. 9. A plot of $P(z,t)$, showing the tendency for atoms to localize in the antinodes of the laser field ($z = 0$ here) after slightly preferential localization at the nodes ($z = \lambda/4$) for short times. The conditions here are $S = 1, \delta = -2\Gamma, \epsilon = 0.0266$, as for Fig. 7. The time sequence is indicated by increasing thickness of the traces.

D. Dopplerons at medium and high laser intensity

At high laser intensity, additional structure in the velocity distribution occurs because of Doppleron resonances, which occur at velocities given approximately by Eq. (43) [38]. Doppleron peaks in the force vs velocity function, shown in Fig. 10(a), result in minima in $P(V,t)$, as shown in Figs. 10(b) and 10(c). In this figure, $P(V,0)$ is rectangular, and the laser moderately intense, with S =25 and $\delta = -5\Gamma$. Over longer interaction times [Fig. 10(c)], many atoms are swept into two central peaks at points where $F(V) = 0$.

At much higher laser intensities, as in the experiments of Tollett *et al.* [27], many more Doppleron peaks occur and the reversal of sign of F_1 becomes more apparent. We will not attempt to model the precise experimental conditions of Tollett *et al.* [27] but will present results with a rectangular initial velocity distribution and constant laser intensity, with $S = 1800$ and $\delta = \pm 30\Gamma$ as in their experiments. Figure 11(b) shows nearly identical results from QDM and SC calculations for red detuning and the experimental interaction time of $132\Gamma^{-1}$, with many Doppleron dips. In this figure and the following, the first-order Doppler resonance ($j = 0$ or $2j + 1 = 1$) at $\approx 38\Gamma/k$ is outside the range plotted for short interaction times, and other peaks in $F(V)$ are labeled by $2j + 1$. The positions of the peaks in $F(V)$ agree to within at least 6% of values obtained from Eq. (44). The positive slope of $F(V)$ at $V = 0$ (positive F_1) leads to heating near $V = 0$, thereby providing another mechanism for a dip near $V = 0$. For very long interaction times [Fig.

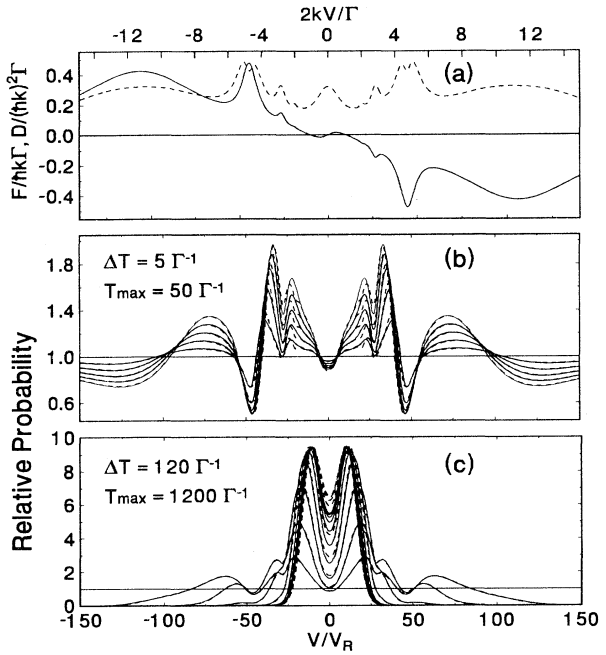

FIG. 10. (a) $F(V)$ (solid line) and $D(V)$ (dashed lines) for high intensity, large detuning [$S = 25$, $\delta = -5\Gamma$, with $\epsilon = 0.0266$ (He*)], showing Doppleron peaks and a small positive slope at $V = 0$. (b) and (c) $P(V,t)$ for short and long interaction times, showing dips where the Doppleron peaks in $F(V)$ occur. SC (dashed) and QDM (solid) results differ near the innermost peak. In the long-time limit, there are peaks near points where $F(V) = 0$.

11(c)], the two peaks at $F = 0$ points appear. Because of the large basis required for the quantum calculations, we show only SC results in Fig. 11(c).

The blue-detuning case, shown in Fig. 12 and in Ref. [27], provides an example of "blue cooling" near $V = 0$, as discussed by Dalibard and Cohen-Tannoudji [36], as well as of Doppleron structures. Over a longer interaction time, again the Doppleron features disappear. Also in this case, the QDM and SC results virtually coincide as far as the QDM calculations were carried. Note in Fig. 12(c) (SC results only) that for long interaction times, the atoms not in the central peak are boiled away. In this calculation, the range of the $F(V)$ and $D(V)$ functions in the FPE integration was extended so that the total probability could be preserved to better than 1% at $T = 3300\Gamma^{-1}$.

This close agreement between two quite different theoretical methods even in the regime of high laser intensity lends credence to both methods. However, we find that there are small but significant discrepancies between QDM/SC results and the experimental data of Ref. [27], as well as with later data in Ref. [46]. These discrepancies are presently being investigated. While the validity of the theoretical methods used here has been shown in the regime of very low intensity (see [23]), detailed confirmation in the high intensity regime is lacking. Close agreement with experimental data may require attention to minor details of the experimental conditions.

E. Recoil energy comparable to or larger than the radiative linewidth

The tiny ripples on top of the nearly Gaussian distribution in Fig. 4(c) are a harbinger of another feature in the velocity distribution that becomes more prominent at larger values of $\epsilon = E_R/\hbar\Gamma$, for which the small velocity increments assumed in deriving the FPE become increasingly invalid. Figure 13 shows typical $P(V,t)$ for $\epsilon = 0.13$ as applies to cooling on the Lyman α transition of hydrogen (see Table I). The peaks at $V = \pm V_R$ are here more apparent. Figure 14 shows even more prominent peaks for $\epsilon = 1/2$. Such peaks in two-level $\sigma^+ - \sigma^+$ Doppler cooling resemble VSCPT effects in three-level $\sigma^+ - \sigma^-$ cooling [10], and in fact have a similar origin. Using the notation $|\eta, q\rangle$, where $\eta = g$ or e, and q is in units of P_R as above, we attribute the peaks at $|V| = \pm V_R$ to the weakly coupled linear combination $\Psi_{WC} = [|g,1\rangle - |g,-1\rangle]/\sqrt{2}$. From Eqs. (6) and (10), $\langle\Psi_{WC}|H_{AL}|e,0\rangle = 0$, but $\langle\Psi_{WC}|H_{AL}|e,\pm2\rangle = \Omega/2\sqrt{2}$, so that Ψ_{WC} is not a completely uncoupled dark state. However, the transition $\Psi_{WC} \rightarrow (e,2)$ is detuned by $2E_R/h$, and for $E_R \approx \hbar\Gamma > -\hbar\delta$ this detuning significantly lowers the loss rate via this pathway. Hence Ψ_{WC} is only weakly coupled to excited states, causing atoms

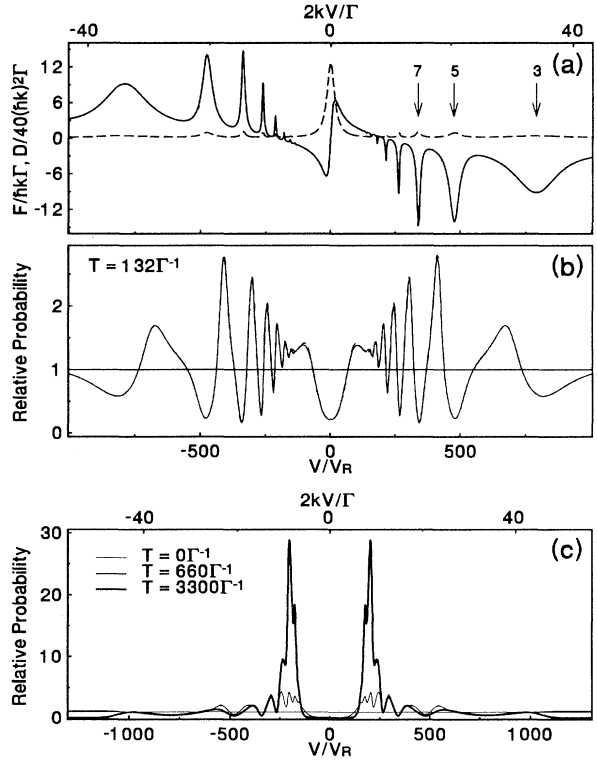

FIG. 11. Results for Li atoms, $\Gamma = 5.87$ MHz, $E_R = 63.2$ kHz, $\epsilon = 0.0108$, for $S = 1800$, $\delta = -30\Gamma$, as in experiments in Ref. [24]. (a) Force (solid) and diffusion (dashed) functions, with a few Doppleron peaks identified by order. (b) SC (dashed) and QDM (solid) results for the experimental interaction time almost coincide. The initial velocity distribution is flat to $|V| = 1200V_R$. (c) SC results for longer times, showing that atoms tend to accumulate near where $F(V) = 0$.

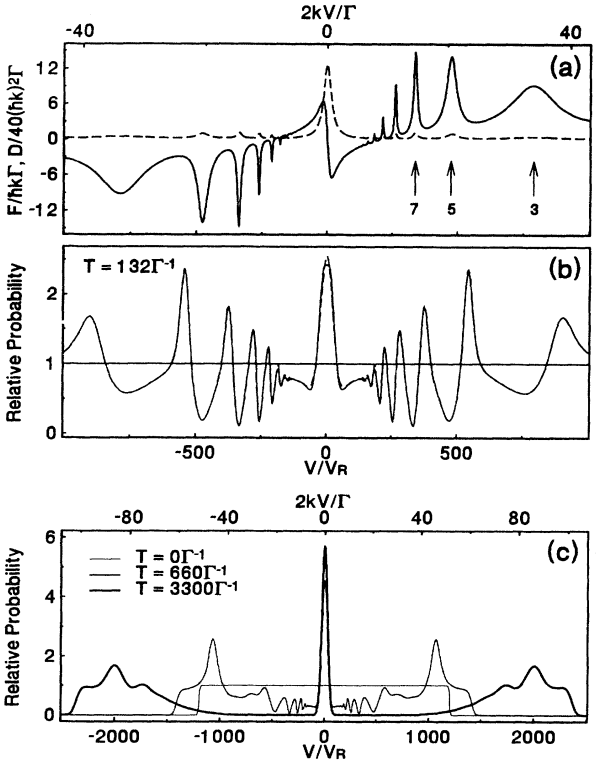

FIG. 12. Results for Li atoms as in Fig. 11, but with $\delta = 30\Gamma$, showing "blue cooling" near $V = 0$. Over long times in (c), most atoms not in the central peak are boiled out of the initially populated velocity range, $|V| \leq 1200V_R$.

to accumulate in it. This viewpoint is corroborated by considering $H_{\text{eff}} = H - i(\hbar\Gamma/2)\sum|e_i\rangle\langle e_i|$ [where H is given in Eq. (2)], over the basis (8). For $\epsilon \approx 1$, we find eigenvalues λ with relatively small $-\text{Im}(\lambda) < 0.01\hbar\Gamma$ for $\text{Re}(\lambda) \approx E_R$ with eigenvectors that correspond closely to Ψ_{WC}, with small additional momentum components that become more important at higher laser intensity. An analytic model would be useful at this point, but we have not been able to truncate the infinite momentum families basis in a fruitful way.

The amplitude of these peaks is found to be maximum for $\epsilon \approx 1/2$, and $\delta = -\Gamma/2$ or $\delta = -\Gamma/4$, as seen in Fig. 14(c). The quasi-VSCPT peaks at $\pm V_R$ persist for an

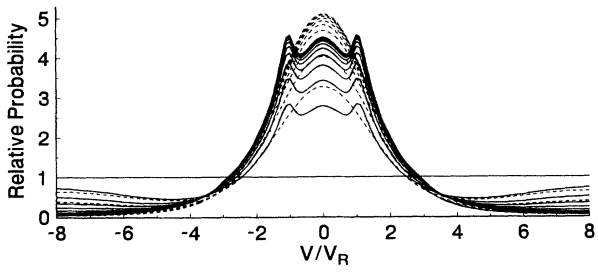

FIG. 13. Doppler cooling on the H Lyman α transition. $S = 0.5$, $\delta = -\Gamma/2$, $\epsilon = 0.13$, $\Delta T = 62.5\Gamma^{-1}$, $T_{\text{max}} = 625\Gamma^{-1}$. Dashed lines are SC results, solid lines QDM results.

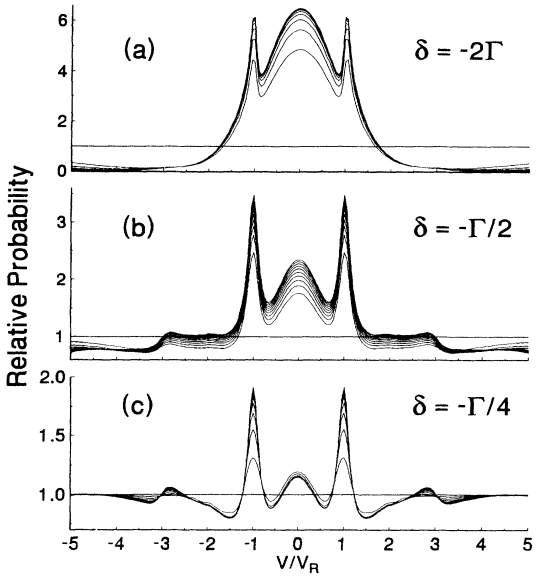

FIG. 14. QDM calculations of two-level Doppler cooling with $\epsilon = 0.5$, $S = 2.0$, δ as indicated. For (a), $\Delta T = 100\Gamma^{-1}$, $T_{\text{max}} = 1000\Gamma^{-1}$; (b) $\Delta T = 50\Gamma^{-1}$, $T_{\text{max}} = 500\Gamma^{-1}$; (c) $\Delta T = 8\Gamma^{-1}$, $T_{\text{max}} = 80\Gamma^{-1}$. The sharp "quasi-VSCPT" peaks at $\pm V_R$ are discussed in the text.

extended time. As Table I shows, the atomic transition that comes closest to meeting the optimum conditions for these sharp peaks appears to be the intersystem line in strontium. At higher laser intensity, coherent superpositions extend over a larger range of momentum, and multiple peaks are observed. When ϵ becomes as large as 2, the peaks at $\pm V_R$ are less intense, as shown in Fig. 15.

Large values of ϵ were considered by Castin *et al.* [6]

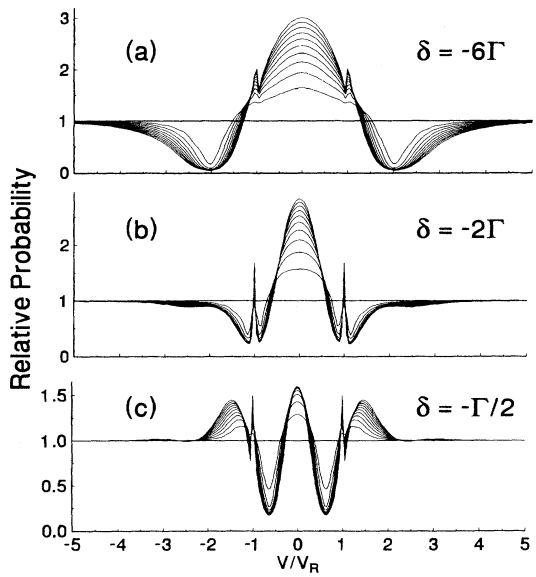

FIG. 15. QDM calculations of two-level Doppler cooling with $\epsilon = 2.0$, δ as indicated. For each plot, $\Delta T = 5\Gamma^{-1}$, $T_{\text{max}} = 50\Gamma^{-1}$. For (a), $S = 3.0$; (b) $S = 2.0$; and (c) $S = 1.0$. Here ϵ is greater than the optimum value for the "quasi-VSCPT" peaks.

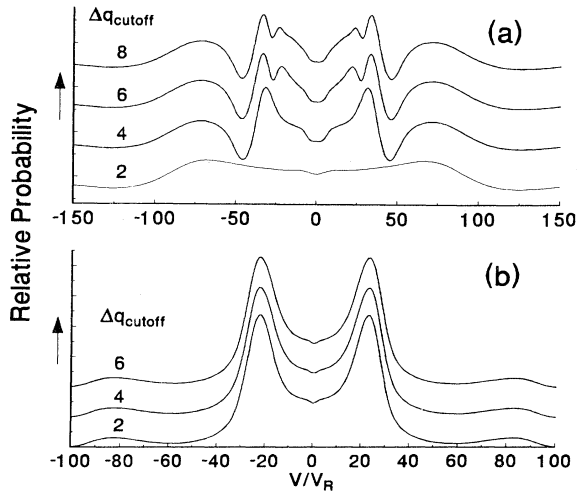

FIG. 16. Effect of the numerical parameter $|\Delta q|_{\text{cutoff}}$, which limits the P-P' range of the off-diagonal elements. (a) Results for the same conditions as in Fig. 9, with $|\Delta q|_{\text{cutoff}}$ ranging from 2 to 8. For $|\Delta q|_{\text{cutoff}} = 4$, the innermost doppleron dip disappears, and for $|\Delta q|_{\text{cutoff}} = 2$, the second innermost dip disappears as well. (c) Results for the same conditions as Fig. 5. There is very little difference between results with $|\Delta q|_{\text{cutoff}} = 2$ and 6, showing that relatively few off-diagonal elements are needed in this case.

for two-level Doppler cooling with $\sigma^+ - \sigma^-$ laser beams. They found that (a) the steady state $\langle E_K \rangle$ approaches a minimum value E_R and (b) the optimum detuning increased with ϵ, such that for $\epsilon = 2$, $\delta = -7\Gamma$ was optimum, with $\langle E_k \rangle$ increasing sharply for smaller detunings. Our results for $\sigma^+ - \sigma^+$ Doppler cooling for $\epsilon = 2$ (Fig. 15) are consistent with this conclusion, in that with $-\delta < 6\Gamma$, atoms with $|V| > 2V_R$ are not swept into the central cooling peak. However, the velocity distribution shows features, such as a narrow cooling peak for smaller detunings, that are not revealed by simply steady-state values of $\langle E_K \rangle$.

F. Choice of $|\Delta q|_{\text{cutoff}}$

The foregoing computational results provide more concrete grounds for discussing the role of the important computational parameter $|\Delta q|_{\text{cutoff}}$. As discussed in Sec. III C, off-diagonal density matrix elements with $\Delta q > |\Delta q|_{\text{cutoff}}$ are neglected. The number of density matrix elements in a calculation is approximately $\mathfrak{N}_\rho = (2|\Delta q|_{\text{cutoff}}+1)\mathfrak{N}$, hence they scale linearly with $|\Delta q|_{\text{cutoff}}$ and with $\mathfrak{N}$. Memory requirements scale linearly with $\mathfrak{N}_\rho$, while CPU times scale approximately quadratically with $\mathfrak{N}_\rho$.

In general, larger values of $|\Delta q|_{\text{cutoff}}$ are required for higher laser intensity and smaller detuning. There is a close relationship between the required value of $|\Delta q|_{\text{cutoff}}$ and the order of H_{AL} in a given feature in the velocity distribution. For example, higher-order dopplerons features successively disappear as $|\Delta q|_{\text{cutoff}}$ is diminished. In Fig. 16(a), we show computational results for the same laser parameters as in Fig. 10. Under these conditions and with $|\Delta q|_{\text{cutoff}} = 6$ or 8, all features are present in the calculation. However, the dips at $|V| \approx 25V_R$ disappear with $|\Delta q|_{\text{cutoff}} = 4$, and the dips at $|V| \approx 50V_R$ disappear with $|\Delta q|_{\text{cutoff}} = 2$. By contrast, Fig. 16(b) shows that the results for $P(V,t)$ for the conditions of Fig. 5(b) are virtually unchanged if all density matrix coherences with $|\Delta q|_{\text{cutoff}} > 2$ are eliminated, which permits a great saving in memory and CPU time.

The calculations for Figs. 3–10 required between 400 and 1120 basis states ($\mathfrak{N}$), and between 3560 and 21 610 density matrix elements. For Figs. 11(b) and 12(b), 2402 basis states and 50 311 density matrix elements were used, and $|\Delta q|_{\text{cutoff}}$ was taken to be 20. In view of the large velocity range in Figs. 11 and 12, the numerical mesh in velocity was $2\hbar k$, or $N = 1$ (Sec. II B), implying simply one family of basis states (see Fig. 1).

IV. QUANTUM EFFECTS IN MULTILEVEL "DOPPLER" COOLING

We now consider $J \to J+1$ transitions with $J > 0$, with $\sigma^+ - \sigma^+$ light. Atoms are initially distributed among the $2J+1$ ground-state magnetic sublevels, but optical pumping will eventually move all the atoms to the $m = J$

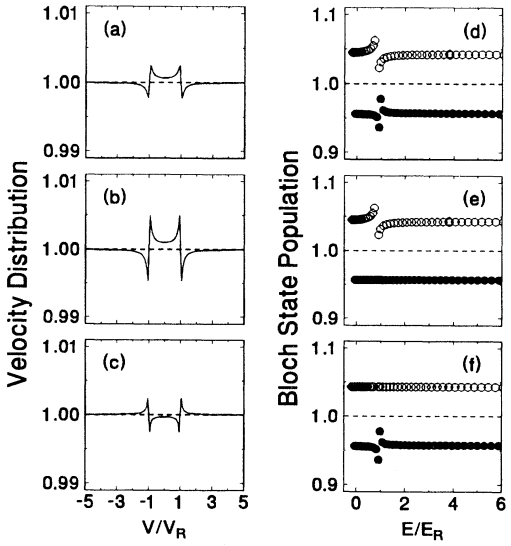

FIG. 17. (a) Velocity distribution and (d) corresponding energy distribution for $S = 0.1$, $\delta = -5\Gamma$, $\epsilon = 0.027$ (He*) $(U_0/E_R = -0.37)$ at $T = 200\Gamma^{-1}$. Open circles mark states in the $m = \frac{1}{2}$ manifold; filled circles mark those in the $m = -\frac{1}{2}$ manifold. In (b) and (e), the structure in the $m = -\frac{1}{2}$ manifold is artificially flattened in both energy and velocity, so only $m = \frac{1}{2}$ anomalies are seen. In (c) and (f), the structure in the $m = \frac{1}{2}$ manifold is flattened, showing that the $m = -\frac{1}{2}$ manifold contribution to the deviations in (a) is opposite in sign to that of $m = \frac{1}{2}$.

state, so the system becomes equivalent to a two-level system. (Unless indicated otherwise, $m \equiv m_g$ in this section.) However, before the system attains this condition, a transient process occurs due to $\Delta m = 1$ excitation and decay, as shown by the additional excitation branches in Fig. 2(a) for the $J = 1/2 \rightarrow 3/2$ case. This transient process involves optical pumping from states in a shallow light-shift potential well to states in a deeper well [see Fig. 2(b) and Eqs. (6) and (25)]. In this section we use the simplest system, $J = 1/2 \rightarrow J = 3/2$, to describe the transient process, and show how it results in transient subrecoil structures in the velocity distribution.

As stated in Sec. II, the most interesting effects occur in the lowest-energy bands when $u = U_0/E_R$ is not much greater than 1. For these effects to be observable, E_R must be relatively large (as for helium or lithium), so that small u does not imply negligible interaction. Under optimum conditions, the effects in $P(V,t)$ discussed in this section are about the same order of magnitude as the effects of slower cooling of atoms in the light-shift potential wells, as shown in Figs. 3(b), 6, and 7, and reported experimentally in Ref. [23]. However, these multilevel effects have not yet been observed experimentally.

The low intensity regime is of special interest, even though the effects are extremely small, because the wave functions are well approximated by trigonometric functions. At low laser intensity (see Fig. 17), we obtain dispersion shapes at $V = \pm V_R$ [Fig. 17(a)]. Similar features are found experimentally and theoretically for lin $\perp$ lin cooling at higher intensity [23] and also in calculations for a $J = 1 \rightarrow 2$ transition with $\sigma^+ - \sigma^-$ laser polarization [47]. In each case, they can be explained by anomalous populations at the edges of the first band gap, and that is the point of view we take here. For the $\sigma^+ - \sigma^-$ case, where the light-shift potential has no spatial variation and the momentum families are finite and closed, Wu and Foot [47] explain these features also (and more simply) in terms of coherent superposition states. This viewpoint is closely related to ours. To lowest order, the states (given explicitly below) at the edges of the first band gap are in fact coherent superpositions of states with $V = \pm V_R$. In the $\sigma^+ - \sigma^+$ case, where the momentum families extend to infinity, the Bloch-Floquet band states provide the most convenient basis for discussion and for calculating higher-order effects.

For low intensity, Fig. 17(d) shows the distribution of population over the eigenstates of the system at $T = 200\Gamma^{-1}$. The overall population of the $m = 1/2$ manifold is greater than that of the $m = -1/2$ manifold, as a result of the optical pumping in σ^+ light. In the $m = 1/2$ manifold, there is a sharp rise (decrease) in the population just below (above) the first band gap, i.e., for states with quantum numbers $(m, n, \nu) = (1/2, 0, \approx 1)$ $[(1/2, 1, \approx 1)]$. [States are labeled as in Eq. (26).] On the other hand, in the $m = -1/2$ manifold, we observe a mirror reflection of this behavior: population is depleted below the first band gap and elevated above it. The deviations in the $m = -1/2$ manifold partly cancel but do not reverse the effects in $P(V,t)$ from the $m = 1/2$ manifold, as is seen from a plot of the separate contributions of each manifold to $P(V,t)$ [see Figs. 17(b) and 17(c)].

These deviations arise from the transient process of excitation from $(J_g, m_g) = (1/2, -1/2)$ to $(J_e, m_e) = (3/2, 1/2)$ and π polarized decay to $(J_g, m_g) = (1/2, 1/2)$. To show why this is so, we consider a very shallow potential, $u \ll 1$, for which the wave function solutions to Eq. (24) may be expanded as a power series in u. (In this subsection, to match to conventional forms of the Mathieu equation [41,42] we will shift the origin of $\zeta = kz$ by $\pi/2$ and take $\mathbf{E} = \hat{\boldsymbol{\epsilon}}_+ E_L \sin(\zeta) e^{-i\omega t} + \text{c.c.}$ [cf. Eq. (3)]. Also we will normalize wave functions $\tilde{\psi}$ to $\int_0^{2\pi} d\zeta |\tilde{\psi}(\zeta)|^2 = \pi$ to first order in u, thus $\psi(\zeta) \sim \tilde{\psi}(\zeta)/\sqrt{\pi}$.) To first order in u, the wave functions $\tilde{\psi}(n, \nu; \zeta)$ for the lowest-energy eigenstates in any band are expansions in $\cos(\zeta)$. For the lowest band,

$$\tilde{\psi}(0, 0; \zeta) = \frac{1}{\sqrt{2}} \left(1 - \frac{u}{8} \cos(2\zeta) + \cdots\right) \tag{45}$$

and for $n > 0$, the lowest-energy states are

$$\tilde{\psi}\left(n, \frac{1 - (-1)^n}{2}; \zeta\right) = \cos(n\zeta) - \frac{u}{16} \left\{ \frac{\cos[(n+2)\zeta]}{n+1} - \frac{\cos[(n-2)\zeta]}{n-1} [1 - \delta(n,1)] \right\} + \cdots . \tag{46}$$

On the other hand, the highest-energy eigenstates in a given band are expansions in $\sin(n\zeta)$. The wave function of the uppermost state of the lowest band is

$$\tilde{\psi}(0, 1; \zeta) = \sin(\zeta) - \frac{u}{32} \sin(3\zeta) + \cdots, \tag{47}$$

and for $n > 0$, the highest-energy states are

$$\tilde{\psi}\left(n, \frac{1 + (-1)^n}{2}; \zeta\right) = \sin[(n+1)\zeta] - \frac{u}{16} \left\{ \frac{\sin[(n+3)\zeta]}{n+2} - \frac{\sin[(n-1)\zeta]}{n} \right\} + \cdots . \tag{48}$$

These low-order approximate wave functions determine the elements for transitions from $m = -1/2 \rightarrow m = +1/2$ due to σ^+ excitation and π decay. For a rough picture, it suffices to consider transitions between states at the edges of the lowest two bands, where the anomalous structure is most pronounced, as in Fig. 17. With the laser field as defined above, the operator for laser excitation on the branch $m_g = -1/2 \rightarrow m_e = 1/2$ is $\Omega \sin(\zeta)/\sqrt{3}$. The decay step is adequately represented by a constant spatial part, since the π polarized fluorescence has an angular distribution that peaks at $\theta = \pi/2$ with respect to the z axis. In computing the matrix elements $\langle \psi(m = -1/2, n, \nu; \zeta) \mid \sin(\zeta) \mid \psi(m =$

$1/2, n', \nu'; \zeta)\rangle$ with the zeroth-order wave functions given above, one has integrals $I(N, M)$, where N and M are integers:

$$\frac{2}{\pi} I(N,M) = \int_0^{2\pi} \sin(N\zeta)\sin(\zeta)\cos(M\zeta)d\zeta = \begin{cases} \pm\delta(M, N \mp 1), & N > 0, M > 0 \\ 2, & N = 1, M = 0. \end{cases} \tag{49}$$

In this way we obtain the transition rates

$$\gamma(-1/2, n, \nu \to 1/2, n', \nu') = \begin{cases} \Gamma'_p & \text{for } (-1/2,0,0) \to (1/2,0,1) \\ \Gamma'_p/2 & \text{for } (-1/2,0,1) \to (1/2,2,0) \\ \Gamma'_p & \text{for } (-1/2,0,1) \to (1/2,0,0) \\ \Gamma'_p & \text{for } (-1/2,0,1) \to (1/2,0,0) \\ \Gamma'_p/2 & \text{for all other band edge transitions,} \end{cases} \tag{50}$$

where $\Gamma'_p = 2S\Gamma/3L$ is the nominal optical pumping rate for the $m_g = -1/2 \to m_e = 1/2$ transition. These transition probabilities are depicted graphically in Fig. 18. In the $m = -1/2$ manifold, the top of the $n = 0$ band is depleted 50% more rapidly and the bottom of the $n = 1$ band 50% less rapidly than band edge states of higher bands, while in the $m = 1/2$ manifold, the top of the $n = 0$ band is populated 50% more rapidly and the bottom of the $n = 1$ band 50% less rapidly than in higher bands. These rates produce the dispersion shapes in the populations shown in Fig. 18 and Fig. 17(d) in the lowest two bands in the limit $u \ll 1$. The rates from states at the edges of the lowest band gap are anomalous because the wave functions have period λ as does the laser amplitude. In lowest order, these deviations do not occur at higher band gaps.

In Fig. 19, we show results with increased laser intensity, $u = 4$. The dispersion structure in the $m = -1/2$ atomic velocity distribution persists because the potential for that manifold is still shallow enough that the first bandwidth is non-negligible. However, in the $m = 1/2$ manifold, the lowest band is narrow and the wave functions vary little within that band. Optical pumping populates this band with essentially no anomalous structure. Now it is the $n = 1$ band in the $m = 1/2$ manifold that has appreciable width, and dispersion structure is noticeable there, producing smaller peaks in the $m = 1/2$ velocity distribution at $V = \pm 2V_R$. The resultant atomic velocity distribution has a peculiar sharp dip at $|V| \leq V_R$.

The "band gap" effect in $m = -1/2$ persists as intensity increases until the $(-1/2,0)$ band becomes narrow and the wave functions do not change character over the band. Figure 20 shows the resultant structure when this happens (at u=7.5). At this intensity, the anomalies in the velocity distribution are dominated by the transfer from the lowest band in the shallow $m = -1/2$ potential to the lowest band in the deeper $m = 1/2$ potential. The double-peaked structure in $P(V,t)$ in Fig. 20(a) occurs

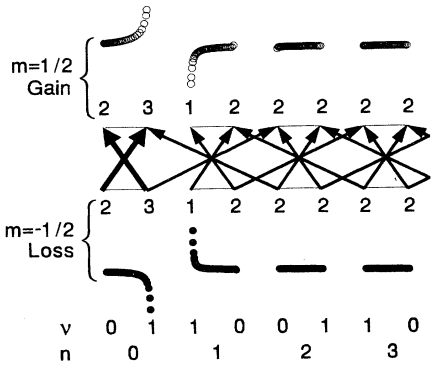

FIG. 18. Schematic diagram of the process by which population is optically pumped from the $m = -\frac{1}{2}$ manifold into the $m = \frac{1}{2}$ manifold, so as to give dispersion-shaped population variations at the edge of the first band gap. (Energy bandwidths are not to scale, nor is the population.) The relative magnitudes of the transition rates at the band edges are shown by the widths of the arrows, while the relative gain or loss of population is labeled numerically. The resultant populations throughout each band are shown schematically for the $m = -\frac{1}{2}$ manifold by filled circles, and for the $m = \frac{1}{2}$ manifold by open circles.

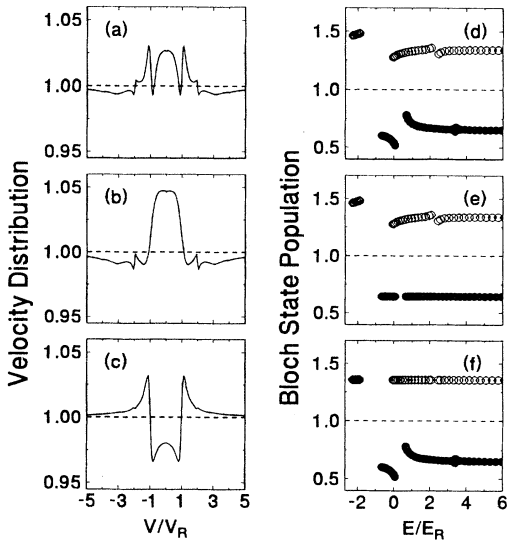

FIG. 19. Same as Fig. 17, but for $S = 1.0$, $U_0/E_R = -3.7$. The sum of the deviations in (b) and (c) produces the highly irregular velocity distribution shown in (a). (d) and (e) show that the $m = \frac{1}{2}$ potential is deeper so the first ($n = 0$) band has become relatively narrow; the population in this first band is elevated, but does not vary much over its width, so there is simply a peak in the velocity distribution in (b). On the other hand, the $m = -\frac{1}{2}$ potential is still rather shallow so there is population variation as in Fig. 16, and dispersion shapes in $P(V)$ (c). Since the peaks in (b) and (c) occur at different velocities, we find three peaks in the total velocity distribution (a).

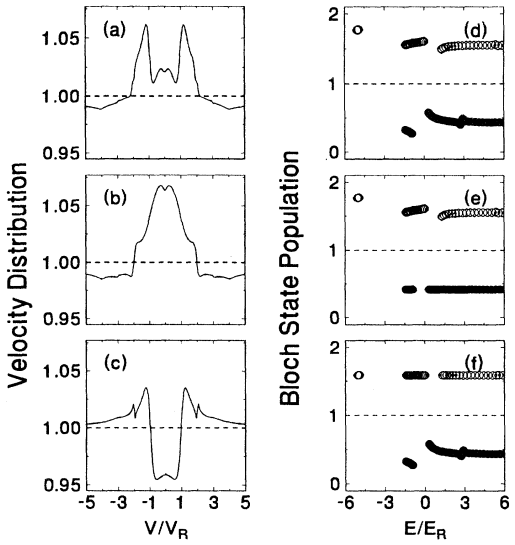

FIG. 20. As in Figs. 17 and 19, but now $S = 2.0$, $U_0/E_R = -7.5$. The $m = \frac{1}{2}$ potential is deeper and the first ($n = 0$) band is extremely narrow. The first and second bands have the largest populations (e) and contribute mostly to the central peak in (b). On the other hand, the first band in the $m = -\frac{1}{2}$ manifold is now sufficiently underpopulated (f) to cause a large dip near $V = 0$ (c), but the second $m = -\frac{1}{2}$ band still contributes to the peaks near $\mid V \mid = V_R$. The sum is a velocity distribution with two peaks as seen in (a).

because a distribution of atoms with a relatively narrow momentum spread is removed and a distribution with a broader spread is added. In addition, the variation of population over the second (n=1) band of $m = -1/2$ contributes to the height of the two peaks in Fig. 20(a).

These results with "Doppler" cooling on a multilevel atomic transition are of interest because the properties of the quantum states in the periodic potential are reflected in the velocity distribution. By way of summary, in Fig. 21, we compare results for a two-level $J = 0 \rightarrow 1$ transition [Figs. 21(a) and 21(c)] with results for a $J = 1/2 \rightarrow 3/2$ transition [Figs. 21(b) and 21(d)] for two values of laser intensity and detuning. In Figs. 21(a) and 21(b), the optical pumping rate $\Gamma_p/2\pi = 0.151$ MHz, while the oscillation frequency of atoms in the wells, $\omega_v/2\pi = 2\sqrt{(E_R U_0)}/h$, is 0.226 MHz. Because of the relatively large ratio $\Gamma_p/\omega_v = 0.66$, the effects of multiple sublevels discussed in connection with Fig. 20 are suppressed, and the $J = 1/2 \rightarrow 3/2$ case resembles the $J = 0 \rightarrow 1$ case. For Figs. 21(c) and 21(d), the well depth U_0 is only slightly greater than for Figs. 21(a) and 21(b), but since the ratio Γ_p/ω_v is only 0.20, the atomic motion samples the potential more effectively. For this intensity and detuning, the quantum effects discussed with reference to Fig. 20 make the results for the $J = 1/2 \rightarrow 3/2$ case quite different from those for $J = 0 \rightarrow 1$. Also, the dip associated with slower cooling rates for atoms in the wells is more sharply defined in Fig. 21(c) than in Figs. 21(a) and 21(b) because of the lower optical pumping rate. Thus "velocity spectroscopy" reveals some rather interesting and novel physics.

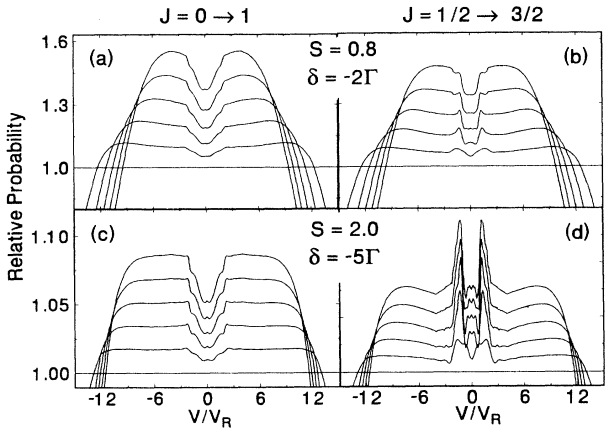

FIG. 21. Comparisons of velocity distributions calculated with the free-particle QDM method for $J = 0 \rightarrow 1$ and $J = 1/2 \rightarrow 3/2$ transitions, each with two sets of laser parameters. The light-shift potential well depths for $m = J$ are about equal in each case [$U_0/E_R = 7.1$ for (a) and (b), and $=7.4$ for (c) and (d)], but $\Gamma/\omega_v = 0.66$ for (a) and (b) and 0.20 for (c) and (d). Therefore the effects discussed in Sec. IV from quantum state transitions become more visible in (d) than in (b).

V. CONCLUSION

Our calculations on two-level and multilevel Doppler cooling (that is, without Sisyphus sub-Doppler processes) have revealed an abundant variety of processes that produce distinctive features in the velocity distribution, particularly when one considers the time evolution for laser parameters that depart from optimum. We have presented computational results that exhibit effects from larger than optimum detuning, slower cooling in the light-shift potential wells, Doppleron resonances, quasi-VSCPT effects, and (for transitions involving more than two levels) the structure of quantum levels in the wells.

A significant conclusion from this work is that excellent agreement can be obtained between quantum density matrix methods and semiclassical Fokker-Planck calculations except in two regimes: (a) atoms with kinetic energy less than the depth of the light-shift potential wells ($E_K < U_0$) and (b) atoms with recoil energy comparable to or larger than the radiative linewidth ($\epsilon = E_R/\hbar\Gamma \gtrsim 1$). Discrepancies in the first regime are associated with the constant velocity parameter used in deriving the force and diffusion functions from the optical Bloch equations, and from spatial averaging in $\bar{F}(V)$ and $\bar{D}(V)$. Methods for solving the FPE without spatially averaged $\bar{F}(V)$ and $\bar{D}(V)$ have not been developed. However, an integral equation approach has been used for lin $\perp$ lin cooling [9], and the Langevin equation has been used with spatially dependent force and diffusion functions [16]. Major deviations between QDM and SC results are to be expected in the regime of large ϵ, where the recoil jump in momentum is typically not negligible compared with the width of the momentum distribution. However, the most dramatic deviations between SC and

QDM results for two-level cooling in the large ϵ regime here are due to velocity-dependent coherent wave function superpositions. It should be noted also that the agreement between QDM and SC results in the small ϵ regime remains excellent at high velocities. Since the excited state was not eliminated in the derivation of SC force and diffusion terms, the condition $V\Gamma^{-1} < \lambda$ does not apply.

The frequent good agreement and notable discrepancies between results from these two prominent methods, SC and QDM, lead to questions about corroboration with experiment. There have been many one-dimensional laser cooling experiments involving transverse cooling of an atomic beam. Some comparisons between experiment and theory regarding effects discussed here have been presented in Refs. [27,46,23]. Decisive comparison between experimental and computational results often requires attention to special experimental conditions, such as the shape of the initial velocity distribution, possible spatial variation of the laser intensity, finite width of the longitudinal velocity distribution (producing a spread of interaction and deflection times), instrumental resolution, and other departures from ideality. We will continue efforts to model these effects theoretically so as to reproduce experimental data, but these questions were outside the scope of the present study.

The approaches used here have obvious extensions. We have already reported certain results for sub-Doppler "Sisyphus" cooling, both with the lin $\perp$ lin configuration and with magnetically induced laser cooling (MILC) [23,22]. A more systematic survey and comparisons with semiclassical results is underway in light of recent results from NIST [48] showing substantially lower temperatures than predicted for lin $\perp$ lin cooling at high intensity by extrapolating low intensity theoretical results [9,22]. Also there are interesting questions about possible new phenomena when the light field as well as the atomic motion must be quantized [49]. And finally, one speculative question at present is whether QDM methods can be usefully extended to more than one dimension.

ACKNOWLEDGMENTS

This work was supported by the NSF, the ONR, the U.S. Department of Education, and by a NATO travel grant. We wish to acknowledge the keen interest and comments of H. Metcalf, and valuable conversations with R. Dum, R. Hulet, C. Xie, and Yu. Rozhdestvensky. Computing time was provided by a grant from The Cornell Theory Center, which receives major funding from IBM and NSF.

[1] See J. Opt. Soc. Am. B **6**, 2019 (1989), special issue on laser cooling and trapping of atoms, edited by S. Chu and C. Wieman.
[2] *Light Induced Kinetic Effects on Atoms, Ions and Molecules*, edited by L. Moi *et al.* (ETS, Pisa, 1991).
[3] *Laser Manipulation of Atoms and Ions*, Proceedings of the International School of Physics "Enrico Fermi," Course CXVIII, Varenna, 1991, edited by E. Arimondo, W. Phillips, and F. Strumia (North-Holland, Amsterdam, 1992).
[4] H. Metcalf and P. van der Straten, Phys. Rep. **244**, 203 (1994).
[5] P. Lett, W. Phillips, S. Rolston, C. Tanner, R. Watts, and C. Westbrook, J. Opt. Soc. Am. B **6**, 2084 (1989).
[6] Y. Castin, H. Wallis, and J. Dalibard, J. Opt. Soc. Am. B **6**, 2046 (1989).
[7] A. Aspect, N. Vansteenkiste, R. Kaiser, H. Haberland, and M. Karrais, Chem. Phys. **145**, 307 (1990).
[8] J. Dalibard and C. Cohen-Tannoudji, J. Opt. Soc. Am. B **6**, 2023 (1989).
[9] Y. Castin, J. Dalibard, and C. Cohen-Tannoudji, in Ref. [2].
[10] A. Aspect, E. Arimondo, R. Kaiser, N. Vansteenkiste, and C. Cohen-Tannoudji, J. Opt. Soc. Am. B **6**, 2112 (1989).
[11] P. Marte, R. Dum, R. Taïeb, P. Zoller, M. Shahriar, and M. Prentiss, Phys. Rev. A **49**, 4826 (1994).
[12] J. P. Gordon and A. Ashkin, Phys. Rev. A **21**, 1606 (1980).
[13] V. Minogin and V. Letokhov, *Laser Light Pressure on Atoms* (Gordon and Breach, London, 1987).
[14] S. Stenholm, Rev. Mod. Phys. **58**, 699 (1986).
[15] J. Javanainen, Phys. Rev. A **44**, 5857 (1991).
[16] J. Javanainen, Phys. Rev. A **46**, 5819 (1992).
[17] K. Berg-Sørensen, Y. Castin, E. Bonderup, and K. Mølmer, J. Phys. B **25**, 4195 (1992).
[18] J. Dalibard and C. Cohen-Tannoudji, J. Phys. B **18**, 1661 (1985).
[19] S. Stenholm, J. Appl. Phys. **15**, 287 (1978).
[20] Y. Castin and J. Dalibard, Europhys. Lett. **14**, 761 (1991).
[21] M. Wilkens, E. Schumacher, and P. Meystre, Phys. Rev. A **44**, 3130 (1991).
[22] T. Bergeman, Phys. Rev. A **48**, R3425 (1993).
[23] M. Doery, M. Widmer, J. Bellanca, E. Vredenbregt, T. Bergeman, and H. Metcalf, Phys. Rev. Lett. **72**, 2546 (1994).
[24] R. Dum, P. Zoller, and H. Ritsch, Phys. Rev. A **45**, 4879 (1992).
[25] J. Dalibard, Y. Castin, and K. Mølmer, Phys. Rev. Lett. **68**, 580 (1992).
[26] K. Mølmer, Y. Castin, and J. Dalibard, J. Opt. Soc. Am. B **10**, 524 (1992).
[27] J. Tollett, J. Chen, J. Story, N. Ritchie, C. Bradley, and R. Hulet, Phys. Rev. Lett. **65**, 559 (1990).
[28] R. Dum (private communication).
[29] E. Vredenbregt and E.-J. Vonken (unpublished).
[30] T. Hänsch and A. Schawlow, Opt. Commun. **13**, 68 (1975).
[31] D. Wineland and H. Dehmelt, Bull. Am. Phys. Soc. **30**, 637 (1975).
[32] D. Wineland and W. Itano, Phys. Rev. A **20**, 1521 (1979).
[33] V. Minogin, Zh. Eksp. Teor. Fiz. **80**, 2231 (1981) [Sov.

Phys. JETP **53**, 1164 (1981)].
[34] N. Bigelow and M. Prentiss, Opt. Lett. **15**, 1479 (1990).
[35] S. Marksteiner, R. Walser, P. Marte, and P. Zoller, Appl. Phys. B **60**, 145 (1995).
[36] J. Dalibard and C. Cohen-Tannoudji, J. Opt. Soc. Am. B **2**, 1707 (1985).
[37] P. Berman and J. Ziegler, Phys. Rev. A **15**, 2042 (1977).
[38] E. Kyrölä and S. Stenholm, Opt. Commun. **22**, 123 (1977).
[39] V. Minogin and O. Serimaa, Opt. Commun. **30**, 373 (1979).
[40] N. Bigelow and M. Prentiss, Phys. Rev. Lett. **65**, 555 (1990).
[41] N. McLachlan, *Theory and Application of Mathieu Functions* (Dover, New York, 1964).
[42] *Handbook of Mathematical Functions*, edited by M. Abramowitz and I. Stegun (Dover, New York, 1965).
[43] N. W. Ashcroft and N. D. Mermin, *Solid State Physics* (Saunders, Philadelphia, 1976).
[44] K. Mølmer, J. Phys. B **27**, 1889 (1994).
[45] J. Dalibard, Thèse d'Etat, Université Paris VI, 1986 (unpublished).
[46] J. Chen, J. Story, and R. Hulet, Phys. Rev. A **47**, 2128 (1993).
[47] H. Wu and C. Foot, J. Phys. B **27**, L677 (1994).
[48] R. Scholten, R. Gupta, J. McClelland, and R. Celotta (private communication).
[49] A. Herkommer, V. Akulin, and W. Schleich, Phys. Rev. Lett. **69**, 3298 (1992).